Thesis for the degree of Doctor of Philosophy

Microstructure and wear mechanisms of textured CVD alumina and titanium carbonitride coatings

SIAMAK SHOJA

Department of Physics

Chalmers University of Technology

Göteborg, Sweden 2022

Microstructure and wear mechanisms of textured CVD alumina and titanium carbonitride coatings

Siamak Shoja

ISBN 978-91-7905-653-7

Doktorsavhandlingar vid Chalmers tekniska högskola
New series nr 5119
ISSN0346-718X

Department of Physics
Chalmers University of Technology
SE-412 96 Göteborg
Sweden
Telephone + 46 (0)31-772 1000

Cover illustration

Some of the main methods used for determination of wear mechanism of machined α-alumina on the rake face of cutting tool inserts. (top-left) SEM image showing the plan-view surface morphology. (top-right) STEM image showing the cross-section of the alumina layer perpendicular to the CFD direction. (bottom-left) Schmid factor diagram for $\{0001\}< 11\bar{2}0 >$ (basal slip system). The full circles represent a loading angle of 45°, corresponding to the transition/sliding zone. The dashed circles are angles 10° away from the nominal value. (bottom-right) Schmid factor map for the basal slip system. All images are for an $(11\bar{2}0)$-textured alumina coating.

Printed by Chalmers Reproservice Gothenburg, Sweden 2022

Microstructure and wear mechanisms of textured CVD alumina and titanium carbonitride coatings

Siamak Shoja
Department of Physics
Chalmers University of Technology

Abstract

The aim of this thesis is to find the reasons behind how the wear performance of hard coatings produced by chemical vapor deposition (CVD) is influenced by their texture, as this is today not fully known. Therefore, differently textured coatings were synthesized, and subsequently analyzed both before and after specially designed machining tests. The main research methods used are analytical electron microscopy, transmission Kikuchi diffraction, electron backscattered electron diffraction, X-ray diffraction, atom probe tomography and Schmid factor simulations.

The microstructure, texture and facet development of the as-deposited α-Al_2O_3 coatings were determined, and the effect of catalyzing gas and diffusion of heavy elements from the substrate were described. After machining tests, terrace formation at the edges is attributed to crystallographic dependent etching. More deformation occurs for the textured coatings in the transition zone, with an associated sub-surface dislocation formation coupled to the number of activated slip systems. The surface morphology in the sliding zone is mainly affected by the surface developed in the previous zones. For the (0001)-textured coating, the observed low wear rate is attributed to homogeneous basal-slip dominating plastic deformation, while for the $(01\bar{1}2)$ and $(11\bar{2}0)$ textures the main deformation mechanism is heterogeneous plastic deformation, causing micro-rupture and abrasion, leading to higher wear-rates.

For titanium carbonitride coatings, the (211)-textured coating exhibits a more significant and non-uniform deformation than (110), which is related to a heterogeneous response of the relevant slip system.

In conclusion, the results presented in this thesis reveal the complex relationships between local wear mechanisms and coating texture. This fundamental understanding can facilitate future development of texture-controlled CVD α-alumina and titanium carbonitride coatings, with the potential of further improving the performance of coated cutting tools.

Keywords: CVD, Coatings, α-alumina, Wear mechanisms, TKD, Electron microscopy, Texture, Plastic deformation, Ti(C,N)

Preface

The work presented in this thesis was carried out in the Division of Microstructure Physics at the Department of Physics, Chalmers University of Technology, during the time period October 2017 – May 2022, under the supervision of Professor Mats Halvarsson, Adjunct Professor Susanne Norgren and Associate Professor Magnus Hörnqvist Colliander.

This research was funded partly by the Swedish Foundation for Strategic Research (SSF), contract ID16-0048, and partly by Sandvik Coromant. The experimental materials were supplied by Sandvik Coromant, Stockholm, Sweden and Seco Tools, Fagersta, Sweden.

List of appended papers

I. *Microstructure investigation of textured CVD alumina coatings*
Siamak Shoja, Nooshin Mortazavi, Erik Lindahl, Susanne Norgren, Olof Bäcke and Mats Halvarsson
International Journal of Refractory Metals & Hard Materials 87 (2020) 105125

II. *Calculated and experimental Schmid factors for chip flow deformation of textured CVD α-alumina coatings*
Siamak Shoja, Oscar Alm, Susanne Norgren, Hans-Olof Andrén, Mats Halvarsson
Surface and Coatings Technology 412 (2021) 126991

III. *On the influence of varying the crystallographic texture of alumina CVD coatings on cutting performance in steel turning*
Siamak Shoja, Susanne Norgren, Hans-Olof Andrén, Olof Bäcke, Mats Halvarsson
International Journal of Machine Tools and Manufacture (2022) 103885

IV. *Rake face wear mechanisms of textured CVD alumina coatings*
Siamak Shoja, Olof Bäcke, Andrea Fazi, Susanne Norgren, Hans-Olof Andrén, Mats Halvarsson
In manuscript.

V. *Schmid factor analysis for chip flow induced plastic deformation of textured cubic carbonitride coatings*
Ren Qiu, Siamak Shoja, Linus von Fieandt, Jan Engqvist, Olof Bäcke, Hans-Olof Andrén, Mats Halvarsson
Submitted to International Journal of Refractory Metals & Hard Materials (8 April 2022).

Statement of contribution

I. As the principal author, I performed results analysis and wrote the paper together with my co-authors under the supervision of my supervisors.

II. As the principal author, I performed the sample preparation, microscopy experiments, results analysis, calculations and wrote the paper together with my co-authors under the supervision of my supervisors.

III. As the principal author, I performed the sample preparation, microscopy experiments, results analysis and wrote the paper together with my co-authors under the supervision of my supervisors.

IV. As the principal author, I performed the sample preparation, microscopy experiments, results analysis and wrote the paper together with my co-authors under the supervision of my supervisors.

V. As the second author, I was involved in planing the work, I performed the sample preparation and microscopy experiments for surface morphology and cross-section investigations, assisted in results analysis and Schmid factor calculations.

List of Acronyms

ADF	Annular Dark Field
AE	Auger Electrons
APT	Atom Probe Tomography
BF	Bright Field
CVD	Chemical Vapor Deposition
DF	Dark Field
EBSD	Electron Backscattered Diffraction
FIB	Focused Ion Beam
HAADF	High Angle Annular Dark Field
IPF	Inverse Pole Figure
PVD	Physical Vapor Deposition
SEM	Scanning Electron Microscope
STEM	Scanning Transmission Electron Microscope
TEM	Transmission Electron Microscope
TKD	Transmission Kikuchi Diffraction
XEDS	X-Ray Energy Dispersive Spectroscopy
XRD	X-Ray Diffraction

Contents

1 Introduction **1**
1.1 Objectives and research questions 1
1.2 Background 2
1.3 Scope of thesis 3

2 Chemical vapor deposition **5**
2.1 Hard CVD coatings 6
2.2 Alumina coatings 7
2.2.1 Alumina phases 8
2.2.2 α-alumina 9
2.2.3 Coating texture 10

3 Metal cutting **15**
3.1 Background 15
3.1.1 Turning operations 16
3.1.2 Workpiece material 17
3.2 Wear mechanisms 18
3.3 Wear types 20
3.3.1 Flank wear 20
3.3.2 Crater wear 21
3.3.3 Plastic deformation 22

3.3.3.1 The wear zones and discrete plastic deformation 23
3.4 Plastic deformation at low and moderate temperatures 25
3.5 Deformation by dislocation slip 26
3.5.1 Burgers vector 28
3.6 Schmid's law 28
3.7 Slip systems in alumina 30
3.8 Slip systems in titanium carbonitride 32

4 Analysis methods **35**
4.1 X-ray diffraction 35
4.2 Scanning electron microscopy 36
4.2.1 X-ray Energy dispersive spectroscopy 38
4.2.2 Electron backscatter diffraction 39
4.2.3 Transmission Kikuchi diffraction 40
4.3 Transmission electron microscopy 41
4.3.1 Imaging modes in TEM 43
4.3.2 Scanning transmission electron microscopy 44
4.4 Focused ion beam/scanning electron microscopy 44
4.5 Atom probe tomography 46

5 Experimental details **47**
5.1 CVD of textured coatings 47
5.2 Turning tests 49
5.2.1 Workpiece materials 49
5.2.2 Cutting conditions 50
5.3 Characterizations 51

6 Results and discussions **57**
6.1 Summary of results 57
6.2 As-deposited textured alumina coatings 58
6.3 Facet analysis 59
6.4 Schmid factor analysis 60
6.5 Wear of α-alumina 62
6.5.1 Overview wear and surface morphology 62
6.5.2 Cross-sectional studies: facet identification, surface chemistry and plastic deformation 64

6.6 Schmid factor analysis for Ti(C,N) 67

7 Outlook **69**

7.1 Future work 69

Acknowledgements **71**

Bibliography **73**

CHAPTER 1

Introduction

This thesis focuses on aspects that are important for a better understanding of the microstructure and wear of multi-layered wear-resistant textured coatings synthesized by Chemical Vapor Deposition (CVD). These coatings consist of Ti(C,N) and α-alumina layers, which are widely used to increase the wear-resistance of cemented carbide inserts used in machining operations.

1.1 Objectives and research questions

The long-term objective of this project is to understand the fundamental degradation mechanisms during metal cutting using α-alumina coatings produced by CVD. This is done by coupling the degradation resulting from machining processes to the detailed microstructure of the coatings, including local texture, surface morphology and grain size. This information is expected to be valuable in order to develop the next generations of CVD coatings.

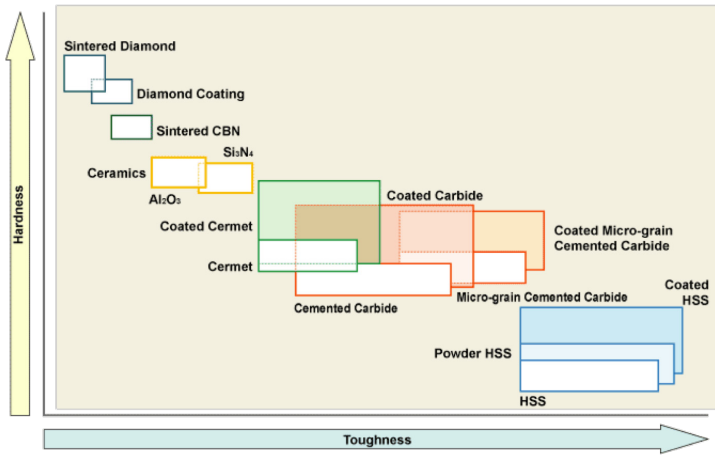

Figure 1.1: Schematic diagram of hardness versus toughness for different hard materials [2].

1.2 Background

The most important properties of materials considered for cutting tool applications are hardness and toughness [1]. Figure 1.1 schematically shows the relationships between hardness and toughness for different types of hard materials. Hardness directly contributes to the wear-resistance of the materials; however, toughness is also needed to withstand the extremely high intermittent forces applied on the tool. It is known that these two parameters are dependent on each other and thus cannot be optimized independently [3]. Other important aspects that should be considered for developing a cutting tool are cost efficiency, environmental issues *e.g.* lowering the usage of lubricant fluids, and the fast development of new advanced materials that are difficult to machine. All these aspects promote dry and high-speed machining. Thus, the demand for wear-resistant coated tools is increasing. Al_2O_3 is an ideal candidate as a coating material for high-speed, dry metal cutting due to its high chemical stability and favorable thermal properties [4, 5]. CVD is commonly employed as a method for industrial deposition of wear-resistant coatings and it has been used for many years for producing thick and uniform Al_2O_3 coatings on cemented carbide (WC-Co) substrates [6, 7]. These coatings are widely used to increase the wear-resistance, and thus tool life, of cemented carbide cutting tools.

The properties of CVD α-alumina coatings have been greatly improved during many years by *e.g.* microstructural refinement by decreasing the fraction of porosities at the interfaces and phase control by optimizing the underlying so-called bonding layers [8–10]. A more recent development of α-alumina

coatings is the deposition of highly textured coatings, which resulted in a further increase of tool life [11]. Enhancing the wear-resistance of the coating materials and prolonging tool life is critical. To improve coating properties, a good understanding of the wear mechanisms is essential. Wear performance of α-alumina coated inserts with various textures have been investigated earlier on both the flank and rake side of the inserts during metal cutting. Flank wear and crater wear are two types of wear on the side and top of the insert that reduce tool life. Crater wear occurs when the workpiece material is in contact with the tool on the rake side. A confluence of plastic deformation, abrasion, and chemical wear is thought to cause the crater wear [12–22]. Different machining parameters such as cutting speed and workpiece material influence the degree and kind of wear on the rake side [19, 21, 23, 24]. It has also been noted that the degree and kind of texture in these coatings affect their performance [11–13]. Furthermore, it was claimed that the principal degradation mechanism is plastic deformation, and that (0001)-textured coatings had the best wear-resistance properties [12, 25]. Due to these results the industrial focus has been on producing (0001)-textured coatings until now. However the reasons for the outperformance of this texture compared to other textures are not entirely understood. This thesis is therefore focused on the microstructure of multi-layered textured coatings (mainly α-alumina) and the influence of wear of these coatings on the rake face.

1.3 Scope of thesis

Several topics of interest for explaining the microstructural and wear variations in multi-layered CVD coatings with various textures have been investigated in this thesis. The first topic concerns the microstructure and texture development of CVD α-Al_2O_3 coatings. This includes the investigation of the chemistry and defects at the α-alumina/bonding layer interface, as well as the texture development of coatings with different textures, and the effect of catalyzing gas on texture development of (0001)-textured coatings (Paper I). The second topic concerns calculations and analysis of Schmid factors for coatings with different textures. This includes plotting Schmid factor diagrams and Schmid factor analysis of fiber-textured coatings in different wear zones for the three most common slip systems activated during typical machining conditions (Paper II). Worn coatings were thoroughly analyzed by investigating the surface morphology of three textured coatings in different wear zones on the rake face (Paper III). By relating a more detailed cross-sectional analysis of the coatings to the surface morphology (Paper IV), the dominating wear mechanisms were identified. These analyses form a knowledge platform that can be used to get a more profound understanding of the microstructure and wear mechanisms of textured CVD α-alumina coatings. Finally, the developed method for investigating the ability of coatings to plastically de-

form using Schmid factor analysis was used to study two different textures of Ti(C,N) coatings (Paper V). Part of the work presented in this doctoral thesis has previously been presented in a licentiate thesis by the same author [26].

To conclude, the insights gained throughout this project will create a better understanding of the characteristics and wear of cutting tool inserts composed of multi-layered CVD textured coatings deposited on cemented carbide substrates.

CHAPTER 2

Chemical vapor deposition

Chemical vapor deposition (CVD) is one of the dominating coating techniques for production of cutting tools. It is a process by which a solid material is deposited from a mixture of gases on a substrate surface. This deposition occurs by chemical reactions between the gas reactants and to some extent between the gas mixture and the substrate surface. These chemical reactions that produce the solid deposit can be started and maintained by heat (conventional CVD), photons (photochemical excitation) or electrons and ions (plasma activated). The use of CVD as a coating technique is well established and it is used for a wide range of materials and for different applications, such as hard wear-resistant coatings, thin film semiconductor devices, and also as corrosion resistant and biocompatible coatings [27–29]. The hard wear-resistant coatings employed in cutting tool manufacturing, are most widely produced by thermally activated processes in hot-wall CVD reactors, where thousands of cutting inserts can be coated in one process cycle. In this thesis, industrial large-scale hot-wall CVD reactors have been used for coating deposition. Figure 2.1 shows uncoated inserts on the graphite tray of a CVD reactor.

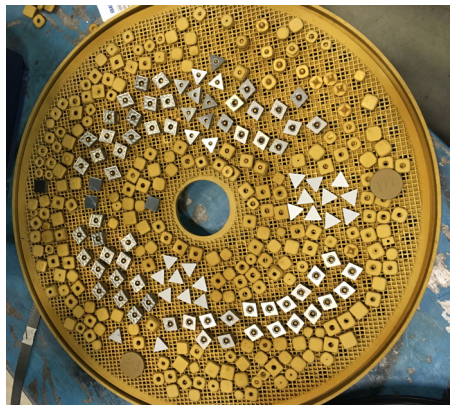

Figure 2.1: Uncoated cutting inserts (silvery) on a graphite tray of a CVD reactor together with some dummy samples (golden).

2.1 Hard CVD coatings

After the invention of cemented carbides, which led to an increased productivity, introducing coated cemented carbides was the second big step that modernized the metal cutting industry. The coating techniques in cutting tool manufacturing are usually CVD and physical vapor deposition (PVD). CVD has a number of advantages as a method for depositing thin films. Some of the primary advantages of this technique are conformal coverage of irregularly shaped surfaces (*i.e.* small details in the geometry of the substrate can be maintained after coating), material can be deposited with very high purity, the deposition rate is relatively high and CVD doesn't need as high vacuum as PVD [30].

Today the most common hard CVD coatings are α-Al_2O_3, κ-Al_2O_3, TiC, TiN and Ti(C,N), while the common PVD coatings that exist today are TiN, Ti(C,N) and TiAlN. Since the conditions in most cutting applications are quite extreme, with temperatures that sometimes exceed 1000 °C and local pressures in the GPa range, these coatings should have several common characteristics [1, 31]:

1. High hot-hardness, which results in less abrasive wear.

2. Chemical inertness, which reduces and limits the oxidation and diffusion wear.

3. Low affinity with the workpiece materials, which results in low cutting forces.

In this work we mainly used multilayered coatings consisting of an inner TiN layer, followed by a Ti(C,N) layer, then a bonding layer of Ti(C,N,O) and finally a layer of α-Al_2O_3. The multilayer coatings were deposited onto a WC-Co substrate. The focus has been on the α-Al_2O_3 layer, which was deposited with three different textures; (0001), $(01\bar{1}2)$ and $(11\bar{2}0)$. A cross-section overview of a typical multilayered coating with (0001) texture is shown in Figure 2.2.

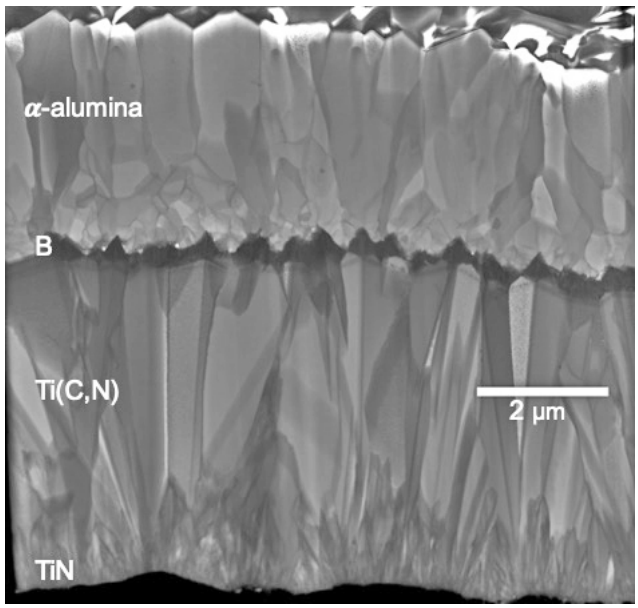

Figure 2.2: Cross-section overview of a multilayered coating with (0001) α-Al_2O_3 texture. The layer between Ti(C,N) and α-Al_2O_3 indicated by letter 'B' is the so-called bonding layer.

2.2 Alumina coatings

Alumina is one of the coatings that can be grown by the CVD technique. CVD Al_2O_3 coatings have been grown from the $AlCl_3$-H_2-CO_2 system since 1970's and are well established and have been frequently examined [5, 7, 9, 32–40]. The formation of solid Al_2O_3 from the gas mixture is based on the hydrolysis of $AlCl_3$ by water as below:

$$2AlCl_3(g) + 3H_2O(g) \rightarrow Al_2O_3(s) + 6HCl(g) \tag{2.1}$$

The water is resulting from the high temperature reduction of CO_2 by H_2:

$$3H_2(g) + 3CO_2(g) \rightarrow 3H_2O(g) + 3CO(g) \tag{2.2}$$

Thus, the overall reaction can be written as

$$2AlCl_3(g) + 3CO_2(g) + 3H_2(g) \rightarrow Al_2O_3(s) + 6HCl(g) + 3CO(g) \quad (2.3)$$

The deposition rate is determined by the formation of water through reaction 2.2 [32–35]. It is possible nowadays to produce dense and hard coatings with a uniform thickness using CVD coating technologies. However, the growth of alumina by CVD is very sensitive to impurities, which usually give heterogeneous crystal growth and poor adhesion. Cobalt, which exists in the substrate, is one of the most important elements that create these problems [36][Paper I], and that is why the WC-Co substrates usually are pre-coated by a coating in the Ti-C-N system in order to eliminate or reduce the effect of Co during the nucleation of Al_2O_3 [5, 7, 9, 37–40].

2.2.1 Alumina phases

Aluminum oxide, also called alumina, has many polymorphs with the chemical composition Al_2O_3. More than 25 crystallographic phases of alumina have been reported [41]. However, there are discussions if they are really new phases or if they simply form by containing absorbed or interlamellar water and impurities that makes new, distorted lattices [42]. In the wear-resistant coatings for cutting tool applications, only stable α-Al_2O_3 and metastable κ-Al_2O_3 are produced by conventional CVD [1, 31]. Many of the alumina phases can be formed by the decomposition of various aluminum hydroxides. A common way to identify different hydroxides and oxides is by using X-ray diffraction [43]. Figure 2.3 shows the classification of aluminum hydroxides.

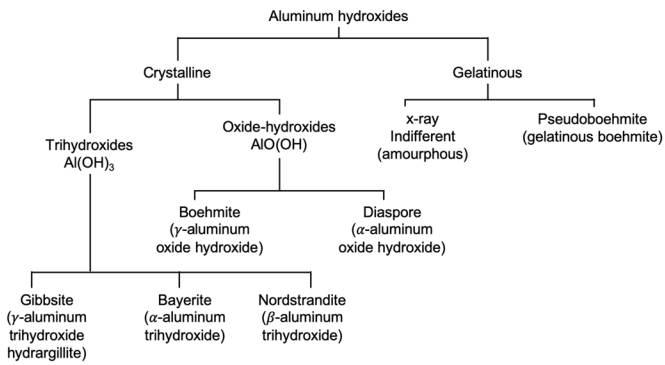

Figure 2.3: Classification of aluminum hydroxides. reproduced from [42]

As shown in the figure, several aluminum hydroxides exist, *e.g.* Gibbsite and Bayerite (both monoclinic). There are two types of aluminum oxyhydroxide, Boehmite and Diaspore; both of them belong to the orthorhombic crystal

Table 2.1: Structural properties of oxides and hydroxides [43]

Phase	Formula	Crystal system	Space group	Molecules per unit cell	Unit axis length, $\times 10^{-1} nm$			Angle	Density g/cm
					a	b	c		
Gibbsite	$Al(OH)_3$	monoclinic	C_{2h}^5	4	8.68	5.07	9.72	$94°34'$	2.42
Gibbsite	$Al(OH)_3$	triclinic	—	16	17.33	10.08	9.73	$94°10'$ $92°08'$ $90°0'$	—
Bayerite	$Al(OH)_3$	monoclinic	C_{2h}^5	2	5.06	8.67	4.71	$90°16'$	2.53
Nordstrandite	$Al(OH)_3$	triclinic	C_i^1	4	8.75	5.07	10.24	$109°20'$ $97°40'$ $88°20'$	—
Boehmite	AlO(OH)	orthorhombic	D_{2h}^{17}	2	2.868	12.227	3.70	—	3.01
Diaspore	AlO(OH)	orthorhombic	D_{2h}^{16}	2	4.396	9.426	2.844	—	3.44
Corundum	Al_2O_3	hexagonal (rhombohedral)	D_{3d}^6	2	4.758	—	12.991	—	3.98

system. Table 2.1 contains structural properties of these oxides and hydroxides [43].

The decomposition sequence of aluminum hydroxides is shown in Figure 2.4.

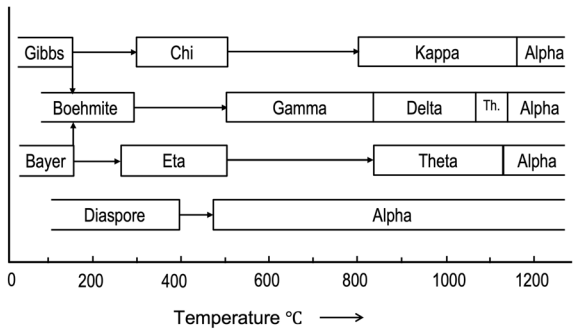

Figure 2.4: Transition sequences of aluminum hydroxides. reproduced from [42]

In CVD applications mostly two modifications of metastable alumina occur, κ-Al_2O_3 and γ-Al_2O_3. Beside these metastable forms of alumina additional phases exist, *e.g.* η-Al_2O_3 (cubic) and χ-Al_2O_3 (hexagonal) [44]. There is only one stable alumina, (α-alumina), and this phase is most relevant to this thesis and the crystal structure of this phase is discussed in the following section.

2.2.2 α-alumina

As mentioned above, α-Al_2O_3 is the only thermodynamically stable form among all alumina phases. It is chemically stable, has a high hardness and a high melting point and low thermal conductivity. In addition to these properties, α-Al_2O_3 has a high resistance against high temperature corrosion, which makes it even more favorable to be used in wear-resistant and high temperature applications. Due to these properties, α-Al_2O_3 is widely used as a coating

material in cutting tool applications and it is normally produced by the chemical vapor deposition method. The crystal structure of α-Al_2O_3, which is called corundum structure, belongs to the trigonal crystal system and has a rhombohedrally centered lattice, with the space group symbol of $R\bar{3}c$. It has an ...ABAB... stacking of closed-packed oxygen ion planes along the c-axis, while the smaller Al ions occupy 2/3 of the octahedral interstitial positions in the O sublattice (...abc...stacking) [45, 46]. This structure is shown in Figure 2.5.

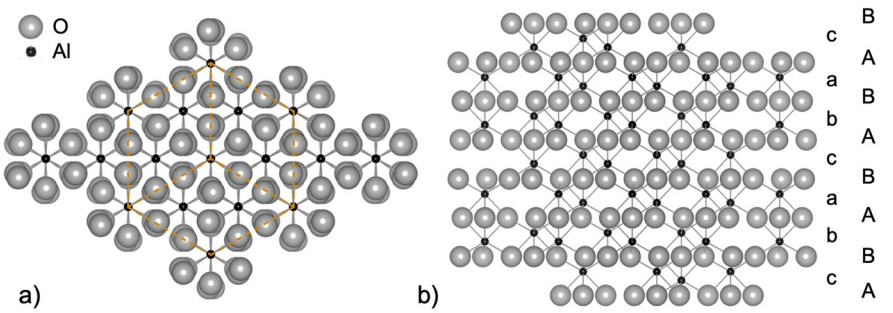

Figure 2.5: The structure of α-Al_2O_3, (a) [0001] projection showing the rhombohedrally centered hexagonal unit cell (b) [$11\bar{2}0$] projection showing the complete stacking sequence of O and Al layers that form *...A-a-B-b-A-c-B-a-A-b-B-c-A...*, reproduced from [46]

α-alumina grown by the CVD method forms a rather large grained microstructure with a grain size of approximately 1–5 µm [9, 37, 39]. Analyzing the texture of CVD grown α-alumina shows that more ordered growth and textured deposition occur at temperatures higher than 1000 °C, while at temperatures around 1000 °C more randomly oriented crystals form [33, 34]. The microstructure of CVD α-Al_2O_3 coatings with three different textures are shown in Figure 2.6. Note the variations in the grain size and the morphology of the alumina grains.

2.2.3 Coating texture

In order to understand the texture of a material one needs to know the crystallographic orientation of its components, *i.e.* how the atomic planes in the bulk, or a volume of the crystal, are oriented with respect to a fixed reference. It is inevitable, therefore, that this characteristic applies only to crystalline materials *e.g.* minerals, ceramics, metals, semiconductors and since most of the materials are polycrystalline, their component units are referred to as grains of the materials [47].

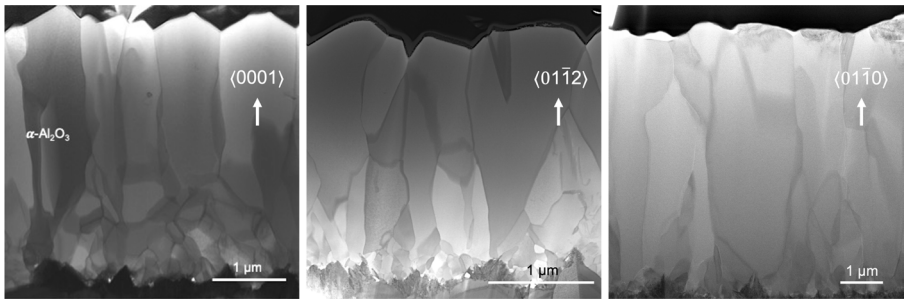

Figure 2.6: Scanning transmission electron microscope (STEM) images showing the microstructure of α-Al_2O_3 coatings grown by CVD with $\{0001\}$, $\{01\bar{1}2\}$ and $\{01\bar{1}0\}$ textures.

Grains in polycrystals can be fabricated, or even occur naturally, with a crystallographic preference of their orientation within a material. This is known as *preferred orientation* or in one word as *texture*. The texture of the material is very important since it greatly affects the properties. In fact, it has been found that texture in most of the cases influences 20 to 50 % of the material properties [48]. Some of the properties that depend on the texture of a material are:

- Young's modulus
- Poisson's ratio
- Strength
- Ductility
- Toughness
- Magnetic permeability
- Electrical conductivity
- Thermal expansion (in noncubic materials)

This great effect of texture on properties of materials is used in materials technology to improve materials properties and produce particular characteristics or behavior of the materials. Textured α-Al_2O_3 coatings are produced by CVD to improve the properties of cutting tools.

There are different methods to measure and understand the texture of a material, *e.g.* X-ray diffraction (XRD) and electron backscatter diffraction (EBSD). By using XRD the texture is determined from numerous individual grains, each

one of them having a discrete orientation. Using the XRD measurements, the degree of texture of different coating layers can be evaluated. One method to evaluate the degree of texture is using texture coefficients, TCs. These are calculated using the intensity ratios between the diffraction peaks (hkl) from a textured coating and the corresponding peaks from a non-textured coating, using Equation 2.4:

$$TC(hkl) = \frac{I(hkl)}{I_0(hkl)} \left\{ \frac{1}{n} \sum \frac{I(hkl)}{I_0(hkl} \right\}^{-1} \tag{2.4}$$

I(hkl) is the XRD peak intensity of the textured coating, I_0*(hkl)* is the non-textured XRD peak intensity from a reference material, and n is the number of peaks considered. As an example, Table 2.2 gives the TC values for two α-Al_2O_3 coatings that were investigated in Paper I.

Table 2.2: Calculated texture coefficients for eight XRD reflections show that the coatings are highly textured. Sample (001) has high texture coefficients for (0 0 0 12), which corresponds to an (0001) texture and Sample (010) has a high texture coefficient for (03$\bar{3}$0), which corresponds to an (01$\bar{1}$0) texture. For coating details, please see Paper I.

TC	(01$\bar{1}$2)	(10$\bar{1}$4)	(11$\bar{2}$0)	(11$\bar{2}$3)	(02$\bar{2}$4)	(11$\bar{2}$6)	(03$\bar{3}$0)	(000 12)
Sample ID								
(001)	0.30	0.59	0.06	0.05	0.09	0.33	0.16	**6.69**
(010)	0.22	0.07	0.13	0.03	0.38	0.06	**7.11**	0.00

The TCs in this case, were calculated based on eight reflections, (01$\bar{1}$2), (10$\bar{1}$4), (11$\bar{2}$0), (11$\bar{2}$3), (02$\bar{2}$4), (11$\bar{2}$6), (03$\bar{3}$0) and (0 0 0 12), which makes the maximum value of the texture coefficient equal to 8. This value corresponds to a perfectly oriented material. In contrast, a value of 1 corresponds to a randomly oriented sample.

XRD measurements will not reveal information about how these grains are distributed in the coating. This extra information can be obtained by EBSD, a method that shows the orientation of each grain, by assigning three Euler angles that describe the grain orientation. These two methods are explained in more detail in chapter 4. The texture of a material can be visualized by pole figures or inverse pole figure maps using the raw data obtained by EBSD (or XRD). Figure 2.7 shows {0001}, {01$\bar{1}$2} and {11$\bar{2}$0} pole figures obtained from EBSD on the surface of an α-Al_2O_3 coating. The intensity at the center of the {0001} pole figure shows that the (0001) plane normals are parallel to coating normal, while (01$\bar{1}$2) plane normals are 57° away from the coating normal, giving a ring of intensity as there is a fiber texture. Similarly, the {11$\bar{2}$0} pole figure have a ring of intensity 90° away. This means that the coating has an (0001) texture.

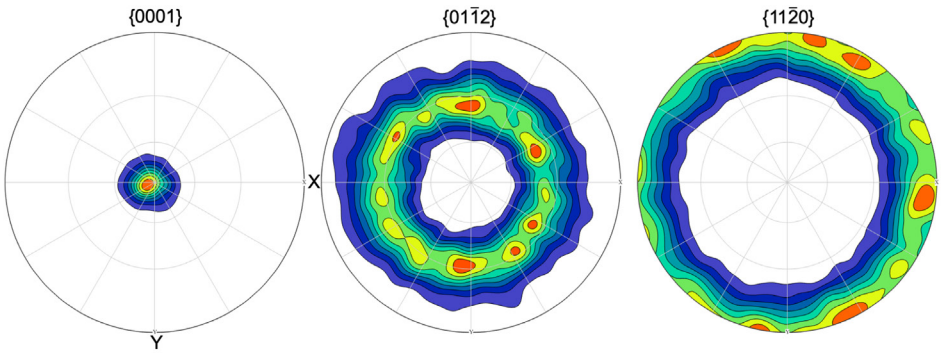

Figure 2.7: Calculated {0001}, {01$\bar{1}$2} and {11$\bar{2}$0} pole figures from EBSD data from an {0001}-textured CVD α-Al_2O_3 coating.

CHAPTER 3

Metal cutting

3.1 Background

In metal cutting operations, also referred to as machining, a thin layer of metal is mechanically removed by a wedge-shaped tool from a larger body (workpiece) in the form of chips [49] to produce a desired workpiece shape and surface. Metal cutting can also refer to other operations, such as shearing of sheet metals, punching of holes or the cropping of lengths from a bar. However, the operation of the tools and processes of separation into two parts is very different than those in chip-forming operations. Thus, in the engineering industry, the term *machining* is used to cover chip forming operations [31]. By combining different metal cutting operations, almost all metals and alloys, hard or soft, cast or wrought, ductile or brittle, with high or low melting points can be machined and complex geometries can be manufactured. The focus in this work is on turning, which is a process utilizing tools with geometrically defined cutting edges to produce rotationally symmetrical components.

3.1.1 Turning operations

Turning is one of the most common machining operations. In this operation, the workpiece material is held in the chuck of a lathe and rotated. The tool is held rigidly in a tool post and (in longitudinal turning) moved at a constant rate along the axis of the bar. Chip formation takes place due to the relative movement between the tool and the workpiece and cuts away a layer of metal to form a cylinder or a more complex profile. A basic schematic for turning of a simple cylindrical workpiece is shown in Figure 3.1. The main cutting parameters in turning operations are: (1) surface cutting speed, v_c (in m/min), defined as the product of the workpiece circumference and its rotational speed at which the periphery of the cut workpiece diameter passes the cutting edge; (2) the feed rate, f_n (in mm/rev), defined as the rate of movement of the tool towards the chuck in relation to the revolving workpiece. This is a main value that determines the quality of the surface and also influences the thickness and formation of the chip against the insert; (3) the depth of cut, a_p (in mm), defined as half of the difference between the un-cut and cut diameter of the workpiece [50].

By knowing the spindle speed (rotational frequency, rpm), the cutting speed v_c may be calculated from the equation 3.1 where v_c is the cutting speed in (m/min), D_m is the machined diameter in mm, n is the spindle speed in (rpm).

$$v_c = \frac{\pi \times D_m \times n}{1000} \tag{3.1}$$

A schematic drawing of some other important parameters is shown in Figure 3.2. The entering/lead angle, KAPR/PSIR respectively (in degrees), is defined as the angle between the cutting edge and the direction of feed. KAPR is an important angle in the basic selection of a turning tool for an operation. This angle can also be defined as the lead angle (PSIR), which is the complement angle to KAPR (PSIR = 90°– KAPR). The angles are schematically shown in Figure 3.2a. The inclination angle λ is the angle with which the insert is mounted in the tool holder, see Figure 3.2b. The final cutting angle with which the cutting edge cuts, will be determined by the insert geometry and inclination in the tool holder. Figure 3.2c schematically shows the angle γ that is a measure of the edge in relation to the cut. The rake angle of the insert itself is usually positive and frequently affects the tool strength, power consumption, finishing ability of the tool, vibration tendency and chip formation [1]. These parameters are also applicable to other cutting operations, like drilling and milling, although the tool and workpiece orientations are different.

There are two types of turning operations, facing and longitudinal turning, depending on whether the tool is fed in a radial or longitudinal direction,

respectively [49]. In this work only longitudinal turning operations were used, as shown in Figure 3.1.

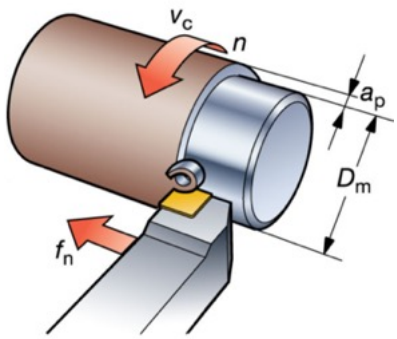

Figure 3.1: Schematic drawing of longitudinal turning operation showing the general set-up for cutting a cylindrical workpiece material and some important features and parameters. (Courtesy of Sandvik Coromant.)

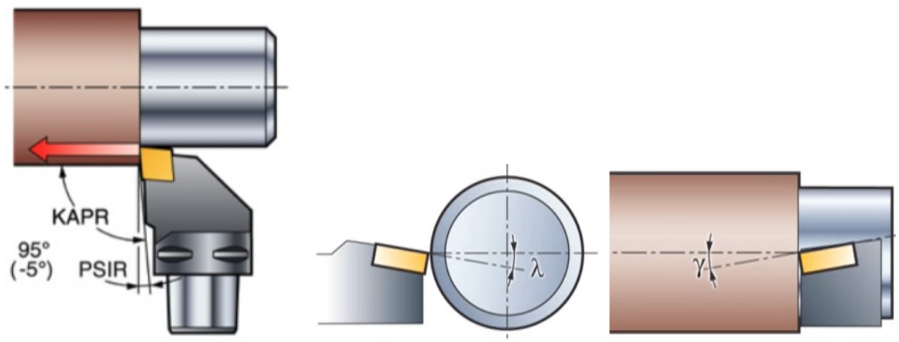

Figure 3.2: Schematics of (a) entering angle (KAPR) and lead angle (PSIR), (b) inclination angle λ, (c) rake angle γ (Courtesy of Sandvik Coromant).

3.1.2 Workpiece material

It is very important to know the type and quality of the material used as workpiece for understanding the wear and tool life in machining applications. The wear of the inserts varies significantly depending on the mechanical and chemical properties of the workpiece. The mechanical properties of the workpiece, such as hardness, yield and tensile strength, will determine the required cutting forces for machining and thus the amount of heat generated that leads to abrasion and plastic deformation.

The chemical properties, like the melting temperature, amount of inclusions and their composition, will also affect the wear of the inserts. This is even more pronounced at high temperatures since the reactivity of the elements and the rate of reaction is higher, due to higher activation energy needed for a reaction to occur [51].

Non-metallic inclusions, which can be found in all types of steels, play an important role in the abrasive wear of the cutting tools, since they usually are quite hard. The most common inclusions in steels are the oxides and sulfides of Ca, Mg, Si and Al. Calcium is often added to the melt during steel production to modify the shape and properties of the inclusions. Ca in the so-called calcium-treated steels, will combine with hard Al_2O_3 particles and create softer and more complex Al_2O_3-CaO particles, which are less abrasive and usually don't form large clusters.

3.2 Wear mechanisms

Wear is usually defined as the removal of material from solid surfaces when one contacting surface moves over another. Thus, both friction and wear are the results of the same tribological contact process that takes place between two moving surfaces. A *wear mechanism* is a classification of the process by which material is removed from the contact surface [52]. The cutting tools have limited life-time at the forces and temperatures generated during the machining process. Several different wear mechanisms are possible during the cutting process and dominate the wear of cutting tools. These mechanisms can be divided into abrasion, dissolution, oxidation and fatigue [1, 52–54].

Abrasive wear

Abrasive wear is caused by hard particles. These hard particles exist in many of the workpiece materials, in different amounts. Steels usually contain hard particles in the form of oxides, nitrides, carbides and oxi-silicides with a hardness similar to the cutting tool. During the cutting process, these hard particles pass along the tool and grind and scratch the tool surface, causing abrasion. In case of coated cutting tools, the hard particles can also be produced by ductile or brittle fracture of the coatings. During abrasion, material removal from a surface can occur by plastic deformation and in this case several deformation modes including plowing, wedge formation and cutting can take place. These modes are schematically shown in Figure 3.3. Plowing occurs as a result of grooves created by plastic flow of the softer material to the sides without removal of material. However, it can happen that material removal also takes place. In this case, ridges that are formed as results of creating grooves, will be

flatter. Plowing can also induce some subsurface plastic deformation and even subsurface cracks can be nucleated. Further continuation of this process can result in propagation of these cracks to the surface and the neighboring cracks and thus, thin wear platelets are created. The amount of this wear debris is small in the case of very soft materials, but for harder materials the wear debris can be significant. In the wedge formation mode an abrasive tip makes a groove in the surface and in this case only part of the softer material will be displaced to the sides and the remaining material builds up a wedge in front of the tip, see Figure 3.3. This type of wear generally occurs when the ratio of shear strength of the interface is high relative to the shear strength of the bulk. In the cutting mode, similar to the metal cutting operation, an abrasive tip with a large attack angle makes a groove and the material is removed in the form of discontinued or continuous-shaped debris particles. Figure 3.4 shows plowing on an α-alumina coating grain, which is observed at the end of the sliding zone where the wear region ends. Note the small ridges formed at the side of the groove. Abrasive wear can be decreased by selecting a harder tool material, although this strategy might fail on other premises.

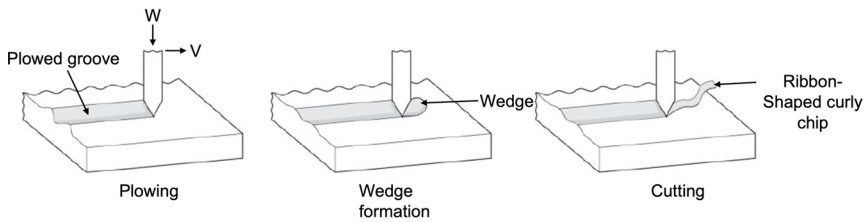

Figure 3.3: Schematic illustration of different modes of abrasion wear mechanism resulting in plastic deformation [55].

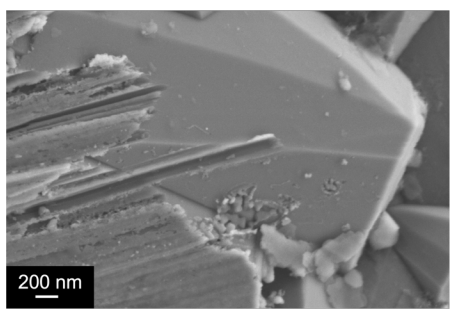

Figure 3.4: SEM micrograph showing the plowing mode of abrasive wear at the end of the sliding zone in an $\{01\bar{1}2\}$-textured CVD α-alumina coating.

Other wear mechanisms

- Dissolution or chemical wear occurs at high temperatures. When the induced temperature during the cutting process at the contact between tool and workpiece is high, some components of the tool material can have a high solubility in the workpiece material, and chemically react with the workpiece during chip formation. In this case, the driving force for diffusion across the tool/chip interface would be high and due to this a considerable amount of tool material can be lost through these chemical reactions.

- When the tool surface is in contact with oxygen, the tool material can be oxidized. The resulting oxide is usually porous and can be easily removed by abrasive particles.

- Fatigue usually occurs in intermittent processes like milling or intermittent turning operations. In this case the tool is subjected to both temperature and stress/load variations, which can lead to failure due to fatigue. This wear usually starts at the so-called comb cracks in the coating, which are shallow cracks along the tool edge.

3.3 Wear types

The aim of coating and WC-Co tool development is to reduce the amount of different types of wear and thus increase the tool life and productivity. There are several different wear types of the cutting tools, which are caused by one or several wear mechanisms. Two common wear types in turning operations are *flank wear* and *crater wear*.

3.3.1 Flank wear

Flank wear (schematically shown in Figure 3.5) is the most common and "preferred" wear type of cutting tool. This is because of the predictable and stable tool life that this type of wear results in. Flank wear is believed to be caused by an abrasive wear mechanism on the flank face of the insert, where temperatures are lower. In this type of wear, the tool material is lost due to the contact against the surface of the workpiece material and by abrasive wear of the coated tool by hard particles. This wear typically begins at the edge line of the tool insert and gradually develops downwards [1, 52]. Figure 3.6 shows flank wear that occurred after two minutes of dry turning of a $\{01\bar{1}2\}$-textured α-alumina coated insert. It can be observed that alumina is worn completely in a narrow region close to the edge of the insert, where the underneath Ti(C,N)

layer is exposed.

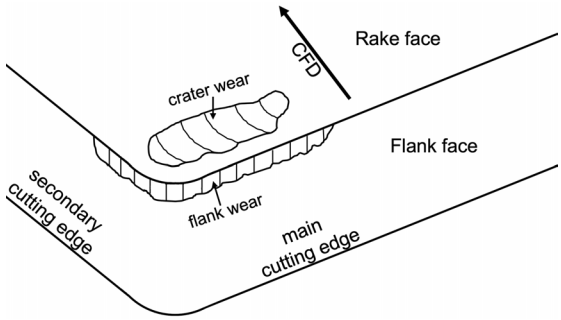

Figure 3.5: Schematic illustration of flank wear and crater wear on a worn cutting tool insert. CFD stands for chip flow direction, which is shown with an arrow.

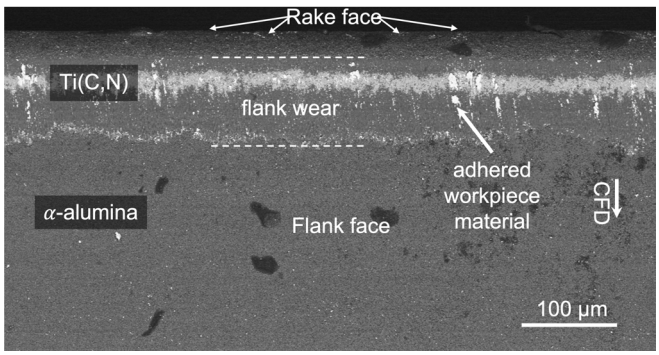

Figure 3.6: Flank wear on a coated cutting tool after two minutes of dry turning. The narrow bright region close to the edge is created by complete removal of the α-Al_2O_3 layer, where the underneath Ti(C,N) layer is exposed. Some adhered workpiece material can be observed (bright spots shown with an arrow). CFD denotes the chip flow direction.

3.3.2 Crater wear

Crater wear occurs on the rake face, where the chip is in contact with the cutting tool insert. This area is also where the maximum tool temperature is reached during the cutting process. This wear appears as a crater, or a groove, on the surface. Crater wear is generally found at the border between the transition and sliding zones (see Figure 3.7 for the wear zones). It normally occurs due to a combination of abrasion and dissolution wear mechanisms

[52]. The crater can be formed either via abrasion of hard particles, which mechanically removes tool material on the rake face, or by chemical reactions happening at the interface between the tool material and chip. However, since the solubility of the common coating materials used in cutting tools is low, chemical reaction and dissolution is limited in the case of coated tools. It has also been shown that a shallow plastic deformation of the coating can take place at the tool/chip contact area [14, 56]. These investigations suggest that plastic deformation followed by ductile fracture and possibly combined with dissolution can be the cause of the crater. Crater and flank wear are schematically shown in Figure 3.5.

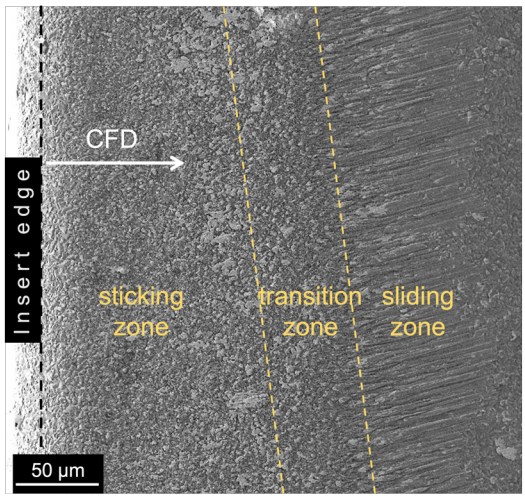

Figure 3.7: SEM micrograph showing the three different wear zones (sticking, transition and sliding) on the rake face of a coated cutting insert. The chip flow direction (CFD) is marked with an arrow, and ridges, at this magnification, are more visible in the sliding zone. sliding zone is located on the sloped part of the insert. (Brighter regions on the surface are adhered workpiece material.)

3.3.3 Plastic deformation

Plastic deformation is one of the wear types that occurs as a result of both high temperatures and high pressures on the tool insert. Temperatures and pressures are high when a hard workpiece material is machined with a high speed and a high feed rate. High hot-hardness is critical for the tools to withstand these conditions and not deform plastically. This type of wear typically occurs on the whole insert when the tool material is softened and the edge of the insert bulges. This may lead to even higher temperatures and

changes in the geometry and chip flow until a critical stage is reached [1, 52]. Figure 3.8 shows the typical plastic deformation that occurs on the coated inserts. Another type of plastic deformation, which is not often discussed, is the plastic deformation that occurs in the coating. This will be discussed in more detail in the subsection below.

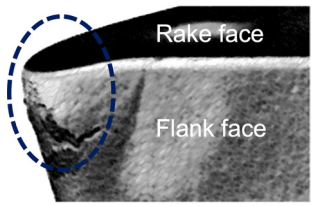

Figure 3.8: Plastic deformation of a cutting tool.(Courtesy of Sandvik Coromant.)

3.3.3.1 The wear zones and discrete plastic deformation

Microscopy examinations of worn alumina coated inserts show that numerous ridges are created parallel to the chip flow direction on the rake face of the tool. Depending on the direction and amount of normal and shear forces, different zones are visible on the rake face, which are shown in Figure 3.7. The sticking zone, which is the region closest to the edge of the tool, is the zone where normal forces are dominant and almost no ridges are visible there. The transition zone is the next zone where shear forces are higher due to the higher flow of the workpiece material, leading to higher temperatures, and ridge formation. The last zone is the sliding zone where the created ridges are extended along the whole region.

It has been observed that the ridges are more pronounced and start to elongate at the end of the transition zone where the temperatures are highest. This suggests that ridge formation is a temperature dependent process and that it develops via plastic deformation at the surface. This can be seen in Figure 3.9, which shows the ridge formation at the end of the transition zone and beginning of the sliding zone, where the originally rough surface has been deformed in the direction of the chip flow.

Studies suggest that the ridge formation involves near surface plastic deformation [14]. This deformation is very shallow and for this reason it is called Discrete Plastic Deformation (DPD). Figure 3.10 shows this type of sub-surface deformation in a worn $\{11\bar{2}0\}$-textured α-alumina coating. The maximum depth of the deformed region is in this case around 200 nm deep.

As the ridge formation continues, it can lead to a ductile fracture of the ridge towards its tail end, which results in tapered ridges along the direction of the

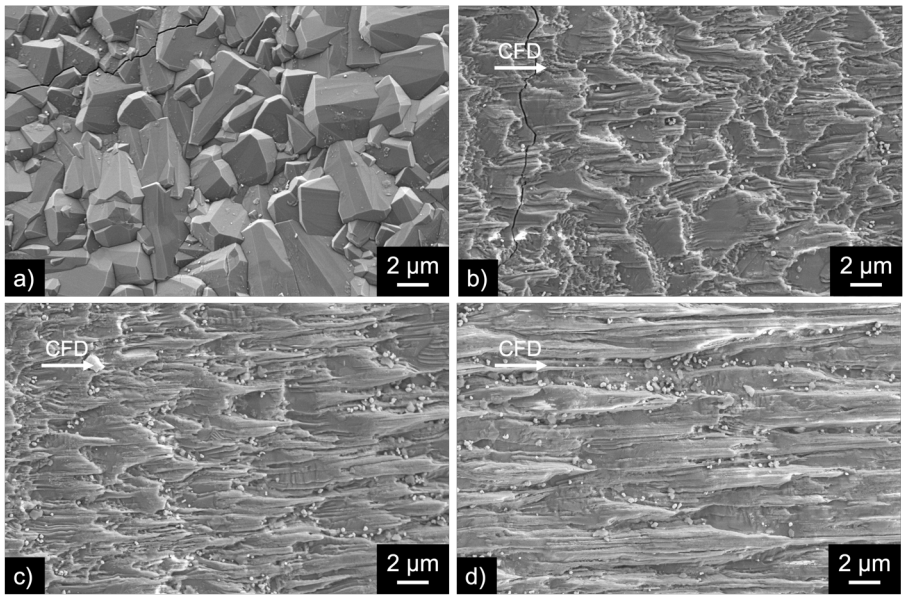

Figure 3.9: Scanning electron microscope images. (a) The as deposited $\{11\bar{2}0\}$ textured α-alumina coating showing the original surface. (b) The worn surface at the beginning of the transition zone showing that the original surface is starting to be deformed in the chip flow direction (CFD) (c) The worn surface at the end of the transition zone showing a larger deformation, resulting in the creation of ridges. (d) The ridges start to elongate at the end of the transition zone and the beginning of the sliding zone, where the contribution of shear forces and the temperature increase. The worn sample was chemically etched in order to remove remaining adhered workpiece material.

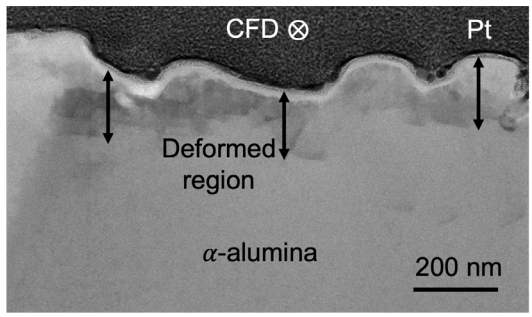

Figure 3.10: STEM bright field image showing the sub-surface deformation (darker contrast) in a $\{11\bar{2}0\}$-textured α-alumina coating after two minutes of dry turning. The chip flow direction is marked (CFD). A Pt layer was deposited on the surface during specimen preparation to protect the sample surface from the FIB milling.

chip. The fractured fragments of the ridge are then removed by the chip [14]. This process is schematically shown in Figure 3.11, which can be compared to Figure 3.9 for a $\{11\bar{2}0\}$-textured α-alumina coating.

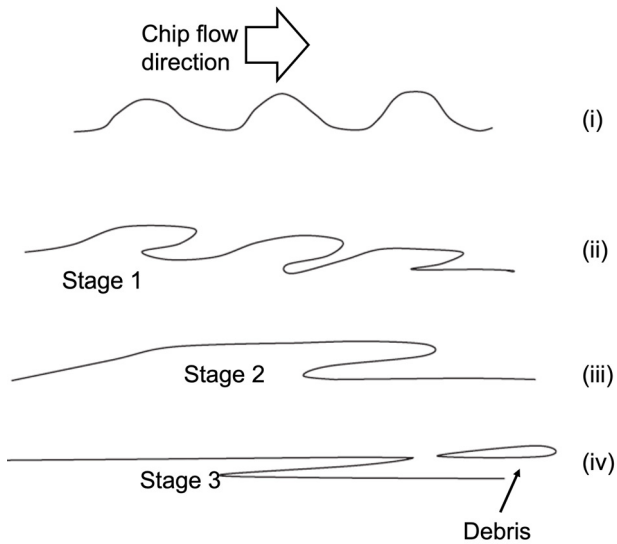

Figure 3.11: Schematic drawing of the ridge formation of hard coatings showing that original surface asperities are plastically deformed in the direction of the chip flow from right to left via sequence (i) to (iv) [50].

3.4 Plastic deformation at low and moderate temperatures

It is known that most of the engineering metals, alloys and ceramics have polycrystalline structures. This means that the atoms in these materials are arranged periodically, formed by the repetition of small unit cells, making up the crystal lattice in grains with different crystallographic orientations. However, the crystal lattices are not perfect and contain flaws, called crystal defects. Different types of defects exist in crystalline materials, *e.g.* vacancies, interstitials and substitutional atoms, which are point defects, dislocations that are line defects, and stacking faults and twin boundaries which are planar lattice defects. The different grains are separated by different types of grain boundaries, and the crystal lattices in a grain boundary region are usually distorted.

Plastic deformation, unlike elastic deformation, occurs by the permanent rearrangement of atoms within the material through the movement of crystal defects. This movement is closely related to the crystal structure and the grain

boundaries [57]. There are different sequences of events that are responsible for plastic deformation and they are called deformation mechanisms. It should be mentioned that these are strongly influenced by temperature. At high temperatures, the deformation mechanisms include thermally activated processes that are time dependent, *e.g.* diffusion and even viscous flow in amorphous structures, whereas at lower temperatures, deformation takes place by processes such as dislocation glide, deformation twinning, crack opening or sliding, or even phase changes [58–60].

The regions for low and high temperatures are relative and depend on the melting point of the material. One parameter that determines whether the temperature is high or low is the homologous temperature, which is defined as:

$$\Theta = \frac{T}{T_f} \tag{3.2}$$

where Θ is the homologous temperature, T is the work temperature in absolute degrees and T_f is the melting point of the material (all temperatures in Kelvin). It is widely accepted that Θ<0.4 is considered as low temperature and Θ>0.4 as high temperature [59, 60]. However, the value of Θ that determines the transition from low to high temperature deformation is not fixed; the transition occurs rather in a range of values.

Among the deformation mechanisms mentioned above, dislocation glide is the most common mechanism that occurs at low and moderate temperatures, and it will be discussed in more detail in this chapter.

3.5 Deformation by dislocation slip

It has been observed that when a material under stress deforms plastically, some fine parallel dark lines start to appear within the grains on a polished surface investigated in the light optical microscope. As the material deforms further, the number of these lines increases and some other, new, lines appear in different directions. These lines are actually very small surface steps that are produced by dislocation slip on crystal planes [61]. These lines are called slip lines and thus dislocation slip on crystal planes is one of the causes of plastic deformation in materials. It was later shown that slip occurs on specific crystallographic planes and in specific crystallographic directions in the crystal structure, and that the slip direction is always parallel to the slip plane [62]. This combination of plane and direction of slip is called *slip system*.

The slip planes are usually the crystal planes that have the highest atomic density in the particular crystal structure, *i.e.* the planes that are most widely spaced. The slip direction is nearly always the direction in the slip plane cor-

responding to one of the shortest lattice translation vectors. The slip systems in a crystal structure is usually known. High symmetry crystals normally have a larger number of slip systems and they are, therefore, usually more ductile. The Taylor model of slip is based on an edge dislocation, which is characterized by a Burgers vector (**b**) perpendicular to the dislocation line and parallel to the slip plane. The stress necessary to move a dislocation is given by Peierls-Nabarro stress τ_P [57].

$$\tau_P = \frac{2G}{1-\nu} \exp\left(\frac{-2\pi h}{b(1-\nu)}\right) \tag{3.3}$$

Here, G is the shear modulus, ν is the Poisson's ratio, h is the interplanar distance of the glide planes and b is the Burgers vector.

Dislocations are line defects with a typical length of the same order as the grain size of the material. There are three kinds of dislocations; edge, screw and mixed dislocations.

- An edge dislocation is formed when an extra half plane is inserted into a perfect crystal. In this case, the Burgers vector **b** is perpendicular to the dislocation line **t**. The edge dislocation can only move perpendicular to the extra half plane, thus in both the **+b** or **-b** directions. Thus, the edge dislocation is limited to one single slip plane. Figure 3.12a shows a perfect cubic structure and Figure 3.12b shows a positive edge dislocation that is formed by insertion of an extra half plane ABCD and the dislocation line (DC) is parallel to the plane. The positive dislocation is shown by the symbol $\perp$ and the negative edge dislocation, when the extra half plane is inserted below ABCD, is shown by symbol $\top$.
- A screw dislocation is formed when the crystal plane ABCD is displaced on one side of the plane relative to the other side in the direction AB. This generates the screw dislocation line DC. The arrangement of the atoms around a screw dislocation is schematically viewed in Figure 3.12c and d. In the case of a screw dislocation, the crystal planes perpendicular to the dislocation form a spiral surface. The Burgers vector **b** is parallel to the dislocation line **t**. When the set of planes undergo clockwise helix along DC then it is called a right-hand screw dislocation; if anti-clockwise it is a left-hand screw dislocation, see Figure 3.12d. Depending on the crystal structure, the screw dislocation can move in several different directions *i.e.* on several slip planes, since no extra half plane is involved in this type of dislocation.
- A mixed dislocation is a combination of an edge and a screw dislocation. It has a Burgers vector that lies at an angle between 0 and 90° from the dislocation line **t**.

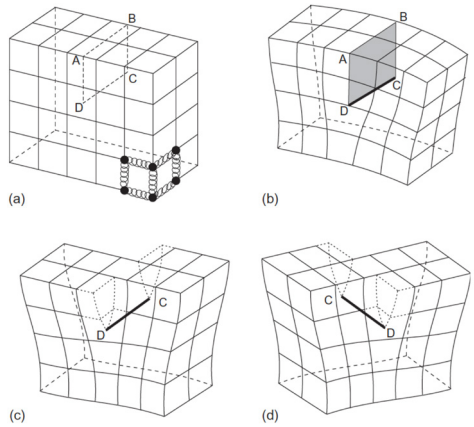

Figure 3.12: (a) A model cubic structure with representation of atoms by filled circles and open circles are "springs" connecting these atoms. (b) An extra half-plane of atoms ABCD create an edge dislocation DC. (c) and (d) The displacement in plane ABCD along the AB direction forms a screw dislocation. Illustration taken from [57]

3.5.1 Burgers vector

Dislocations are defined by their Burgers vector, **b**, and are always associated with the direction of their dislocation line **t** (a vector property). In Figures 3.13a and 3.14a, the Burgers circuit passes along the atoms forming a closed loop (MNOPQ) on a plane perpendicular to a dislocation line. If the same loop is formed in a perfect crystal, 3.13b and 3.14b, then one step still remains when the circuit is closed. The vector that is required in order to go back to the starting point of the circuit is called the Burgers vector (**b**). For an edge dislocation, Figure 3.13, $\overrightarrow{QM}$ is the Burgers vector. It is perpendicular to the dislocation line.

A screw dislocation, Figure 3.14b, has the closing vector $\overrightarrow{QM}$ parallel to the dislocation line. Depending on the kind of dislocation, its Burgers vector **b** can thus be either perpendicular or parallel to the dislocation line **t**. However, in reality most of the dislocations are of mixed type and **b** lies at an arbitrary angle to the dislocation line **t**.

3.6 Schmid's law

As discussed in the previous sections, the movement of dislocations usually occurs through slip (or glide) along crystal planes. Schmid (1924) showed experimentally that slip in a given crystal and system occurs when the shear

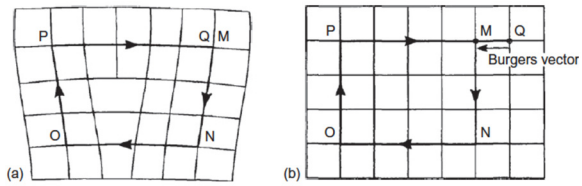

Figure 3.13: (a) Burgers circuit MNOPQ with positive edge dislocation and (b) the closure of QM with Burgers vector **b** to form a perfect crystal [57]

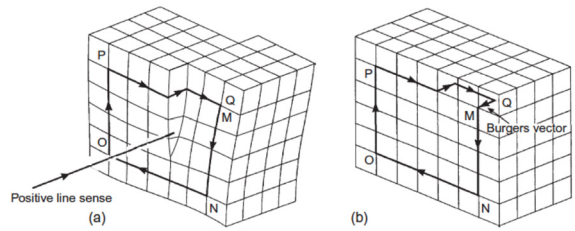

Figure 3.14: (a) Burgers circuit for a left-handed screw dislocation. (b) The closure of the defect in a perfect crystal [57]

stress resolved on the slip plane in a slip direction reaches a critical value, the critical resolved shear stress. Neither the stress normal to the slip plane nor the shear stress on the slip plane perpendicular to the glide direction have any effect on the slip. Thus, the choice of moving mechanisms is dependent on the critical resolved shear stress (τ_{crss}), material structure and the obstacles that hinder this movement. The dislocations are usually quantified by dislocation density, ρ and defined as the length of all dislocation lines per unit volume.

$$\rho = \frac{l}{V} \tag{3.4}$$

Where l is line length (m), V is volume in m^3; the unit of ρ is m^{-2}.

The resolved shear stress (τ_R) is the shear component of an applied stress that influences directly onto a slip plane. The resolved shear stress is calculated from the applied tensile stress σ on the sample ($\sigma = (P/A)$, where P is the applied load and A the sample cross-section area) by equation 3.5, with symbols shown in Figure 3.15.

$$\tau_R = \sigma \cos\phi \cos\lambda = \sigma m \tag{3.5}$$

The term $m = \cos\phi \cos\lambda$ is called *Schmid factor*. When τ_R is sufficiently high as to initiate slip, it is called critical resolved shear stress (τ_{RC}), thus:

$$\tau_{RC} = \sigma_0 \cos\phi \cos\lambda \tag{3.6}$$

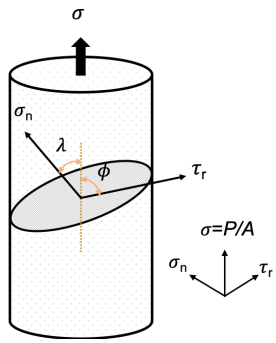

Figure 3.15: Schematic of applied stress on a crystal together with the normal and shear stress components on the slip plane.

where σ_0 is the single crystal yield strength. When several active slip systems exist, slip is more probable to begin in the system with the highest Schmid factor. If the load direction is such that the Schmid factor value is zero for a slip system, dislocation slip is impossible. The maximum value of the Schmid factor is 0.5 because of the relation between the angles ϕ and λ.

3.7 Slip systems in alumina

The possible slip systems of α-alumina (sapphire), with a corundum crystal structure, will be discussed here since that is central in this work. The mechanical behavior of sapphire single crystals has been studied extensively. Snow and Heuer have reviewed the observed slip systems and those listed in Table 3.1 are considered the most prominent ones [63].

Table 3.1: Most prominent slip systems of Al_2O_3 [63].

Slip planes	Most prominent slip systems
Basal	$\{0001\}<11\bar{2}0>$
Prismatic	$\{11\bar{2}0\}<\bar{1}101>$
	$\{11\bar{2}0\}<\bar{1}100>$
Pyramidal	$\{\bar{1}012\}<10\bar{1}1>$
	$\{\bar{1}101\}<10\bar{1}1>$

In hexagonal materials where the c/a ratio is large (c/a=2.73 for alumina(trigonal, with hexagonal axes) [45]), basal slip is generally easily activated. Prismatic slip, $\{11\bar{2}0\}<\bar{1}100>$, operates when the applied stress axis is perpendicular to the c-axis [64]. Pyramidal slip, either $\{\bar{1}012\}<10\bar{1}1>$ [65] or $\{\bar{1}101\}<10\bar{1}1>$ [66, 67], is promoted when the applied stress is parallel to the c-axis, and the

Table 3.2: Dislocation slip systems in Al_2O_3 [63].

Reported slip plane		Possible slip systems
Structural indices	Mineralogical symbol	
0001	c	$\{0001\}\ 1/3< 11\bar{2}0 >, < 10\bar{1}0 >$
$10\bar{1}0$	m	$\{10\bar{1}0\}\ 1/3< \bar{1}2\bar{1}0 >$
$11\bar{2}0$	a	$\{11\bar{2}0\}\ 1/3< \bar{1}101 >, 1/3< 2\bar{2}01 >,$ $< \bar{1}100 >, 1/3< 1\bar{1}02 >$
$01\bar{1}2$	r	$\{01\bar{1}2\}\ 1/3< 2\bar{1}\bar{1}0 >, 1/3< 0\bar{1}11 >, 1/3< \bar{2}021 >$
$10\bar{1}1$	s	$\{10\bar{1}1\}\ 1/3< \bar{1}2\bar{1}0 >, 1/3< \bar{1}101 >$
$2\bar{1}\bar{1}3$	n	$\{2\bar{1}\bar{1}3\}\ 1/3< \bar{1}101 >, < 01\bar{1}0 >$
$2\bar{1}\bar{1}2$	w	$\{2\bar{1}\bar{1}2\} < 01\bar{1}0 >, 1/3< \bar{1}012 >$
$4\bar{2}\bar{2}3$	v	$\{4\bar{2}\bar{2}3\} < 01\bar{1}0 >$

resolved shear stress for basal or prismatic slip is zero. Other slip systems are also reported for Al_2O_3 as listed in Table 3.2, including the most favorable slip systems and possible Burgers vectors [63]. The positions of these slip planes are shown on the stereographic projection for Al_2O_3 in Figure 3.16 and the angles between the planes can be measured.

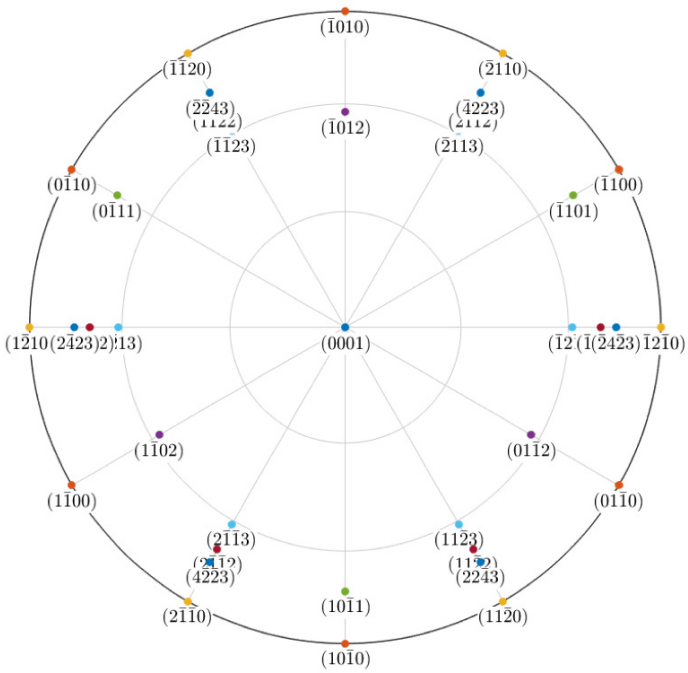

Figure 3.16: Upper hemisphere stereographic projection of α-alumina illustrating the position of all possible slip planes listed in Table 3.2.

It should be mentioned that activation and slip of these reported slip systems is dependent on the brittle to ductile transition temperature (≈1100 °C for alumina [68]). It has been shown that at elevated temperatures (600°– 1000°), basal slip with the Burgers vector of $\mathbf{b}_B$=0.476 nm is the slip system that is first activated, while prismatic slip with the Burgers vector $\mathbf{b}_{Pr}$=0.822 nm is more difficult to activate and pyramidal slip ($\mathbf{b}_{Py}$=0.513 nm) is the most difficult slip system to activate [68].

3.8 Slip systems in titanium carbonitride

The slip systems in Ti(C,N) have received little attention. Ti(C,N) is a solid solution composed of TiC and TiN. Both TiC and TiN have a sodium chloride (rock salt) structure, where the corner of the face-centered-cubic (FCC) lattice formed by C atoms (or N atoms in the case of TiN) located at the position (1/2, 0, 0) of the FCC, lattice formed by Ti atoms, as illustrated in Figure 3.17. Because TiC and TiN are isomorphous, the carbon atoms in the TiC lattice can be replaced by nitrogen atoms in any ratio, allowing for the creation of a continuous sequence of solid solutions Ti($C_{1-x}N_x$) where 0 < x < 1.

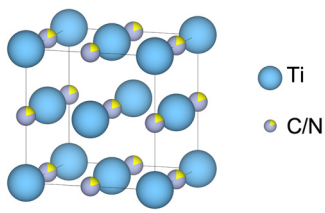

Figure 3.17: FCC rock salt crystal structure of Ti(C,N) [69]

The possible slip systems of different materials with sodium chloride structures have been investigated thoroughly and have been reported to be $\{100\}< 1\bar{1}0 >$, $\{110\}< 1\bar{1}0 >$ and $\{111\}< 1\bar{1}0 >$. Some materials with rock salt structure are brittle and have predominantly ionic bonding, such as AgCl [70], NaCl [71], MgO [72], LiF [73] and alkalihalides [74]. However, cubic carbonitrides (MX, M=Ti, V, Ta, Nb, Zr, Hf, X=C,N) are very strong and have predominantly covalent bonding with some metallic contribution. Dislocation movement and the reported possible slip systems, however, vary depending on the material and the temperature at which the deformation occurs [70–72, 75, 76]. Studies have reported $\{110\}< 1\bar{1}0 >$ slip system as the easiest slip system for cubic carbonitride materials to be activated at low temperatures as a result of lower critical shear stress (CRSS) [75, 76]. However, as an example, it has been reported that the possible slip systems of titanium carbide (TiC) with rock salt structure have three modes where $\{110\}< 1\bar{1}0 >$ slip occurs at low temperatures, $\{110\}< 1\bar{1}0 >$ and $\{111\}< 1\bar{1}0 >$ at intermediate temperatures

and $\{111\}< 1\bar{1}0 >$ at temperatures above the brittle to ductile transition temperature [76]. Schematic drawings of the mentioned slip planes and the slip direction are illustrated in Figure 3.18. Possible slip systems of two textures of Ti(C,N) using Schmid factor analysis in metal cutting conditions have been investigated in Paper V.

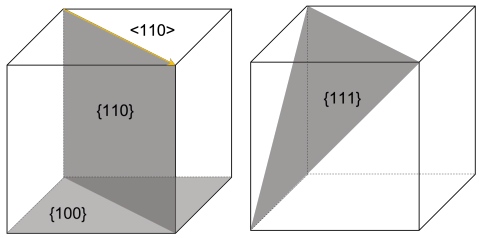

Figure 3.18: Schematic drawing of a Ti(C,N) cubic unit cell where the main slip planes and slip direction are shown.

CHAPTER 4

Analysis methods

The characterization techniques used for microstructure and wear investigations are discussed in the following sections. The focus will be on electron microscopy techniques, which are powerful for materials characterization. In addition, X-ray diffraction (XRD) is also discussed, as it was used to analyze the coating textures.

4.1 X-ray diffraction

In XRD [77, 78] usually a crystalline or powder sample is illuminated by essentially monochromatic X-rays. The incident X-rays are then diffracted by the crystals (sample) according to Bragg's law and the diffracted beam is detected by an X-ray detector. Bragg's law is stated in equation 4.1, where λ is the wavelength of the X-rays, d_{hkl} is the interplanar distance between the (hkl) atomic planes and θ is the Bragg angle.

$$\lambda = 2d_{hkl} \sin \theta \tag{4.1}$$

During a θ - 2θ scan, the sample and the detector rotate with an angular speed of ω and 2ω respectively, while the diffracted intensity (I) is recorded continuously as schematically illustrated in Figure 4.1. The result, which is the

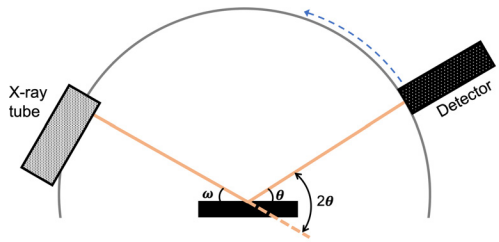

Figure 4.1: A schematic drawing of the geometry of an X-ray diffractometer.

intensity I as a function of 2θ, is generally presented as a diffractogram. This diffractogram can be compared with stored powder diffraction files (PDF:s) for phase identification. The reflection angle (2θ) of the peak positions is identified and θ is then used to calculate interplanar spacings of the crystal. The peak intensities may be used in the determination of the texture of the coating. X-ray diffraction can also be utilized to give information about the structure of amorphous or nanocrystalline materials [78].

4.2 Scanning electron microscopy

Scanning electron microscopy (SEM) is the most frequently used electron microscopy technique for materials characterization. It is possible to examine a wide range of materials, including bulk specimens, at a nanometer to micrometer scale, which is of great value in experiments that require relatively large examined areas, compared to what can be analyzed in, for example, the transmission electron microscope (TEM), see below [79]. A schematic drawing of a conventional SEM is shown in Figure 4.2.

The electrons in an SEM are emitted from an electron source and accelerated in the electron gun. The most commonly used electron sources are the thermionic W and LaB_6 filaments and the field emission tip used in field emission guns (FEGs). The SEMs used in this work are equipped with FEG electron sources. The electron gun is important because it affects the spatial resolution. The electron gun accelerates electrons to energies typically in the range of 1–30 keV. Electromagnetic lenses focus the electrons to a very fine probe (typically a few nanometer) that is scanned across the sample surface. The spot size is determined by the condenser lens, while the objective lens controls the focus of the beam onto the specimen. These lenses also affect the spatial resolution. Interactions between the specimen and electrons result in a variety of signals that are emitted from different penetration depths [80], as shown in the schematic illustration in Figure 4.3.

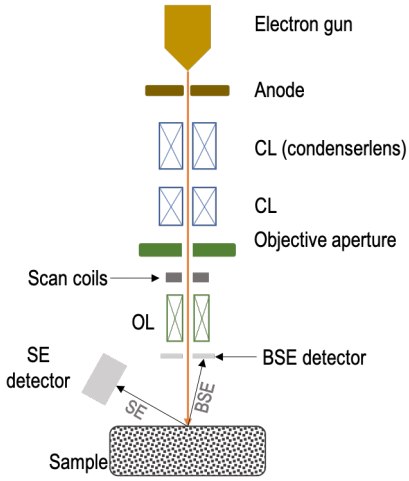

Figure 4.2: Schematic diagram of a SEM, reproduced from [80].

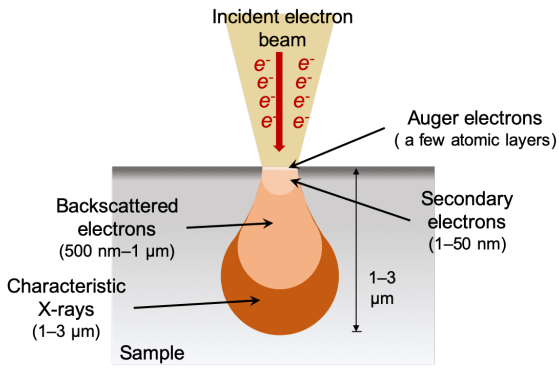

Figure 4.3: Schematic of electron beam/sample interaction showing the origin of the emitted signals.

Among these generated signals, secondary electrons and backscattered electrons, that are used for imaging, and characteristic X-rays, that are used for chemical analysis, are the most important.

- Secondary electrons (SEs) are outer shell electrons that are ejected from atoms of the specimen as a result of inelastic scattering of primary beam electrons. SEs have a low kinetic energy ($\leq$50 eV), therefore only the electrons from a very shallow depth can escape from the specimen surface [79]. As a result, these low energy electrons give useful information about the topography of the surface, and carry topographical contrast infor-

mation. One application of detecting secondary electrons in the SEM is imaging of the topography of 3-dimensional objects, giving information about *e.g.* shape, size and surface roughness.

- Backscattered electrons originate from the incident beam and escape from the specimen after a series of elastic and inelastic scattering events. They have an energy range of $0<E_{BSE}\leq E_0$, where E_0 is the energy of the incoming beam. The higher energy of BSEs results in larger escape depths, up to several hundreds of nanometers. This results in a lower spatial resolution in BSE images as compared to SE images. BSE images show compositional contrast and the intensity in a backscattered image of a polished surface depends mainly on the atomic number (Z) of the analyzed material [79]. Thus, the image will have Z-contrast. Areas with a high Z give a high yield of backscattered electrons and scatter more electrons back towards the detector, and will, thus, appear brighter in the image, as compared to areas with low Z. High Z atoms scatter more electrons of the incident beam. The interaction volume in the specimen increases with increasing accelerating voltage, thus, the BSE spatial resolution decreases with increasing accelerating voltage.

4.2.1 X-ray Energy dispersive spectroscopy

In addition to the imaging capabilities of the SEM, the instrument is also adapted to provide chemical analysis of the elements in a sample using X-ray energy dispersive spectroscopy (XEDS), also known as EDS or EDX [79, 80]. XEDS utilizes element characteristic X-rays, which are emitted as a result of the interaction between the primary electron beam and the atoms of the specimen. Characteristic X-rays are then generated when incident electrons are scattered inelastically and make an atom of the sample ionized by knocking out a core electron of the atom. The ionized atom will return to its ground state when the vacant electron site is filled by an electron from an outer shell falling to the lower energy level. The excess energy is emitted in the form of a characteristic X-ray photon. By detection and measurement of the energies of the emitted X-rays, it is possible to obtain qualitative and quantitative chemical information about the specimen. A qualitative chemical analysis is possible by plotting the number of counts against the photon energy and comparing the peak energies of the spectrum with reference values of the different elements. When performing a quantitative analysis, the background part of the X-ray spectrum, produced as bremsstrahlung, must be subtracted. The atomic number (Z), absorption (A), and fluorescence (F) influence the quantitative analysis. Thus, the so-called ZAF-correction must be done, which is usually implemented by analyzing calibration samples, which are standard samples with known composition.

The lateral spatial resolution in the analysis of a bulk sample is in the order of 1 μm while for thin foil TEM specimens it is $\approx$10 nm. Therefore, it is possible to make detailed chemical analysis of different samples, including thin foils, which makes this method a fast, inexpensive and basically non-destructive (can be destructive for thin foils) analytical technique.

4.2.2 Electron backscatter diffraction

It is important to understand the crystallography of a material in order to determine the structure and its possible relations to the properties. A more complete picture of the sample and thus a better understanding of the performance of the material is developed if the microstructure and the crystallography of a sample are coupled. Electron backscatter diffraction (EBSD) is a method that provides links between the microstructure, crystallography, and physical properties of a material. EBSD is used in the SEM and for two main purposes. One is to determine the orientation of the crystals in the specimen (grains) by the use of diffraction patterns generated when the focused electron beam interacts with a crystalline specimen. The other application is the identification of micrometer or submicrometer crystalline phases through determination of characteristic crystallographic parameters, such as crystal plane spacing, angles between planes, and crystal symmetry elements [81].

EBSD is most often used for bulk samples in the surface region of crystalline materials. The specimen surface to be examined is required to be tilted towards the detector by approximately 70° with respect to the plane perpendicular to incident beam, in order to obtain sufficient intensity in the EBSD pattern. When an electron beam enters a crystalline solid, the primary electrons may be scattered by means of elastic and inelastic scattering events. They produce diffusely and inelastically scattered electrons emitted in all directions. This means that there can be some electrons, which as a last event will arrive at the Bragg angle of some lattice planes. These electrons may then be diffracted according to Bragg's law, forming Kossel cones, which contain crystallographic information about the material. Since the electrons used for EBSD have very small wavelengths, the Bragg angle will typically be less than 1°. The consequence of the small Bragg angles involved in electron diffraction is that the intersections of the two Kossel cones with the EBSD camera appear to be nearly straight and parallel lines. These lines are called Kikuchi lines. The pair of lines is called a Kikuchi band and the spacing between the lines is proportional to an angular distance of 2θ, which is inversely proportional to the interplanar spacing [82]. Figure 4.4 schematically shows the setup and the basic geometries of EBSD.

The Kikuchi patterns recorded on the detector (electron backscatter pattern,

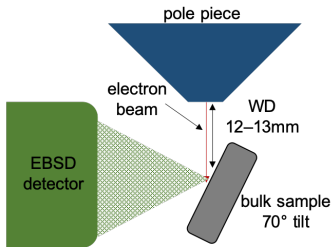

Figure 4.4: Schematic of EBSD geometry.

EBSP) are then automatically indexed by a computer system, which detects the Kikuchi bands and their intersections and measures the spacing and angle between the bands and thus, the crystallographic information at each point is extracted. The crystallographic information is stored by assigning three Euler angles with respect to the sample coordinates. These Euler angles can be used to store all possible rotations of the crystals, as schematically shown in Figure 4.5.

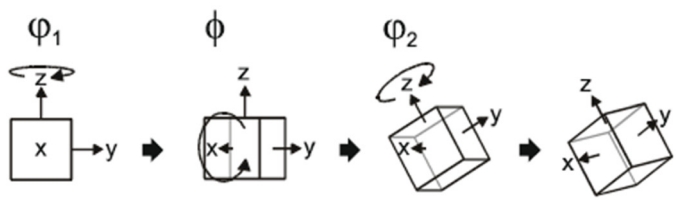

Figure 4.5: Schematic drawing of the three Euler angles: $\phi 1$, Φ, $\phi 2$ representing the rotations about z-axis, x-axis and (the new rotated) z-axis, respectively.

4.2.3 Transmission Kikuchi diffraction

The transmission Kikuchi diffraction (TKD) technique is a variant of the conventional EBSD method, which was developed recently [83]. TKD analysis is performed on thin foils instead of bulk samples, and the transmitted electrons are registered on the camera. This technique, that is also a SEM-based method, offers an improvement in spatial resolution (as high as 2-4 nm) compared to EBSD (typically 50 nm) [84]. The thin foil specimen for TKD analysis is placed horizontally, or at small angles (0–20°), tilted in the opposite direction of the EBSD detector and at low working distances (≈4 mm). A schematic of a TKD setup is shown in Figure 4.6.

Since the diffraction is occurring in a small volume of the electron transparent sample, much higher spatial resolution than for bulk samples can be obtained.

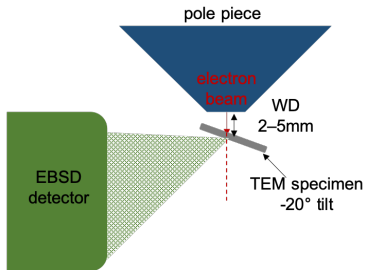

Figure 4.6: Schematic of TKD setup.

The diffraction patterns are mostly generated from the bottom side of the lamella [85]. Standard TEM lamella preparation procedures are followed in the FIB in order to get cross-section samples for crystallographic analysis of the α-alumina coatings. A 20° pre-tilted holder, 30 keV accelerating voltage and 3–5 mm working distance were used in this work. The selected electron probe step size mainly depends on the features and the grain size of the material studied. A step size of 15–40 nm was used for analyzing the CVD α-alumina coatings. An advantage of using TKD over EBSD for α-alumina coatings was that the structure and crystallographic information of the very small grains at the interface towards the Ti-rich layer could be unveiled as a result of the high spatial resolution. Cross-sections vs plan views, makes it also possible to analyze the crystal orientations or texture of the coating as a function of coatings height. This allows us to investigate how the coating texture develops from the interface to the top of the coating, which was used in Papers I,III,IV. The quality of the obtained TKD data is influenced by the sample quality. In order to achieve the best quality, there should be no grain overlaps along the electron beam path.

4.3 Transmission electron microscopy

Transmission electron microscopy (TEM) is one of the most powerful and unique techniques for materials characterization. TEM investigations generally include the use of imaging, electron diffraction and microanalysis for observing and analyzing features of microstructure at micron to nanometer scale with good resolution [86]. The method is, however, costly and can be quite time consuming, as compared to SEM. The information is obtained by detecting the electrons that are transmitted through the specimen or by detecting the X-rays emitted from the specimen. Therefore, the specimen used in TEM analysis should be an electron transparent lamella with the thickness typically in the range of 20–200 nm. The optimal thickness of the lamella depends on many factors, such as the type of analysis, grain size, energy of the

incoming electrons, etc. The electron beam usually has an energy of 100 to 300 keV. The high energy is necessary to provide good spatial resolution and the highest resolution obtained in a TEM is today (with correctors) about 0.5 Å. A schematic drawing of a TEM is shown in Figure 4.7.

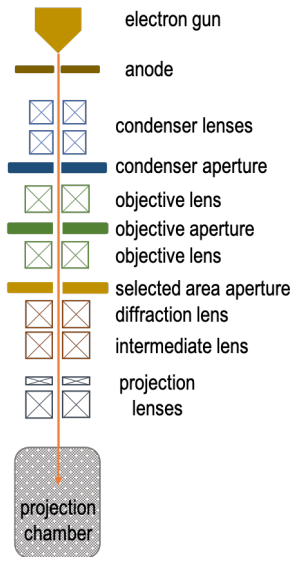

Figure 4.7: Schematic of a TEM column showing the positions of the lenses and apertures, reproduced from [86].

The illumination system usually consists of two or three condenser lenses. The first lens (C1) is strong and collects electrons over a large solid angle and focuses them into a small, demagnified image. The second condenser lens (C2) is much weaker and project this image onto the specimen. These lenses are equipped with condenser apertures that control the beam divergence.
The image forming system consists of an objective lens and an objective aperture. The objective lens forms the image of the sample, as well as the diffraction pattern. The objective lens also determines the resolving power of the microscope and is, thus, the most crucial component of the TEM. The lens is made strong in order to minimize the spherical aberration. The projection lenses magnify the image, or the diffraction pattern, that is produced by the objective lens. Finally, the image, or the diffraction pattern, is projected on to a fluorescent screen where it can be observed. The image or the diffraction pattern can also be viewed or recorded digitally by a CCD camera mounted below the fluorescent screen. The TEM column is equipped with stigmators for correction of condenser and objective lens astigmatism. The FEI Titan 80-300 TEM/STEM used in this research is equipped with a C_s corrector. The C_s corrector is used to correct spherical aberration since it cannot be corrected by

electromagnetic lenses. By suppressing spherical aberration, larger condenser aperture can be used and thus, the diffraction effect will be decreased.

4.3.1 Imaging modes in TEM

Standard TEM imaging techniques were used in this work: (i) bright field (BF) and (ii) dark field (DF). These techniques give diffraction contrast in images from crystalline samples. The difference between these two techniques is the position of the objective aperture that is inserted in the back focal plane of the objective lens where the electron diffraction pattern is formed. A single diffraction spot is selected to contribute to the image. If the aperture is placed around the direct electron beam, and all other spots are blocked, the image is called a *bright field (BF) image*. The condition is shown in Figure 4.8(a). In a BF image, grains that only diffract weakly, or areas that have low crystallinity, will appear with bright contrast. A BF image will, in addition, show mass-thickness contrast, *i.e.* areas with low density or low atomic number (Z) will appear with bright contrast [86, 87]. This method is quite useful for detecting crystal defects. The reason behind this is that the diffraction contrast is modified locally by the defects.

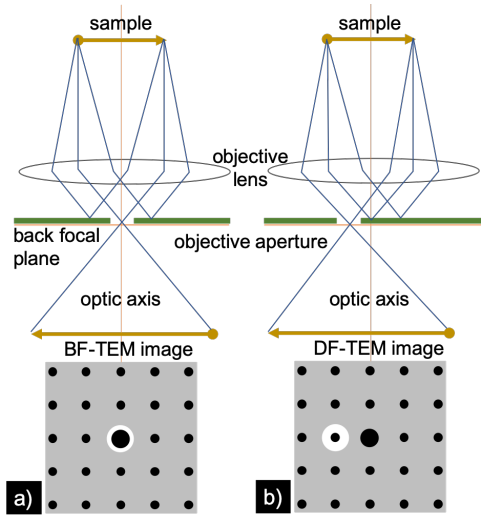

Figure 4.8: Schematic drawing of TEM imaging modes. The position of the objective aperture (gray) in the electron diffraction pattern (black dots) in the back focal plane of the objective lens is shown in side view (top), together with the projected diffraction pattern perpendicular to the optic axis (bottom), including the position of the objective aperture for (a) BF and (b) DF imaging. Reproduced from [86].

If the small objective aperture is instead placed around a diffraction spot

that contains electrons that have been diffracted by a specific set of atomic planes, the image is called a *dark field (DF) image*. This condition is shown in Figure 4.8(b). Bright areas in dark field images are regions that contribute to the specific diffraction spot in the objective aperture, while all other regions appear dark [86, 87]. DF imaging is usually used for highlighting certain grains or defects in the image.

4.3.2 Scanning transmission electron microscopy

Scanning transmission electron microscopy (STEM) requires that a TEM is modified by adding a scanning coil setup in the electron column. STEM imaging is different from TEM imaging in the way that instead of using a parallel beam as in TEM, a finely focused electron probe scans over the sample in a raster fashion. In STEM the images are acquired by different detectors instead of using apertures. However, the same principle is used. The bright field (BF) detector is placed in the electron beam path and only collects the forward scattered or the unscattered electrons through small angles $<\approx 3^{\circ}$, which also depends on the so-called camera length. Annular dark field (ADF) detectors are used for ADF images, which are complementary to the BF images. These detectors are like concentric circles, where the annular areas collect differently scattered electrons. As a result, they provide diffraction and atomic number contrast. A high Z contrast is obtained at the outer circle of (or outside) the ADF detector, by use of a high angle annular dark field (HAADF) detector. A schematic illustration of the position of the different detectors is shown in Figure 4.9.

4.4 Focused ion beam/scanning electron microscopy

Focused ion beam (FIB) microscopy has been used widely in fundamental materials studies over the past decades. The FIB is an instrument similar to the SEM in setup, however, it uses ions instead of electrons. This technique offers flexible micro-machining in addition to imaging [88]. This micro-machining (milling) allows the preparation of site-specific cross-sections, of for example coatings and thin films, with more accuracy and less artifacts in comparison to mechanically prepared cross-sections. One of the most important application of the FIB is the preparation of site-specific and high-quality TEM lamellae with thicknesses less than 100 nm [88].

A basic FIB instrument consists of a vacuum system, specimen chamber, detectors, gas delivery system, a liquid metal ion source (LMIS) which can produce a bright and focused beam, ion column, specimen stage, gas inlets and a com-

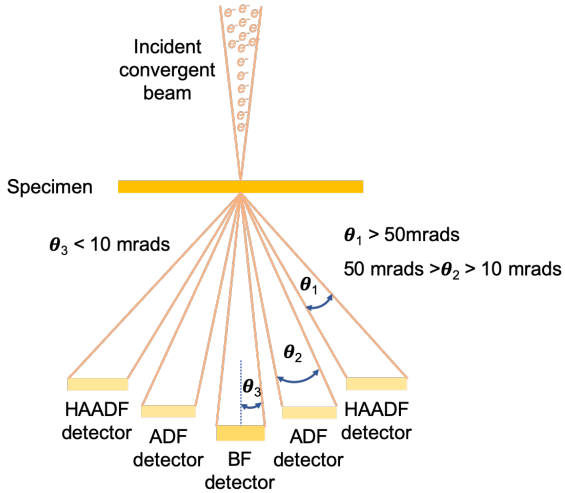

Figure 4.9: Schematic illustration showing the position of detectors for BF, DF and HAADF imaging in STEM.

puter to run the instrument. Today, the most common FIB instruments have a dual-beam FIB/SEM platform. The dual-beam instrument operates by focusing gallium ions on the sample in addition to a focused electron beam. The basic setup of the dual-beam FIB-SEM is shown in Figure 4.10. As shown in

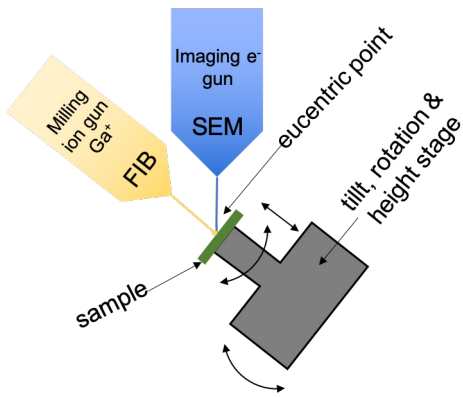

Figure 4.10: Schematic illustration of a FIB-SEM setup.

the figure, the electron column is vertical and the ion column is inclined at an angle, usually 52° or 55°, depending on the manufacturer. Thus, it is possible to perform electron/ion imaging, deposition of platinum (or tungsten, carbon or SiO_2) as protective films or support structures, as well as milling procedures in the same instrument.

4.5 Atom probe tomography

Atom probe tomography (APT) is a destructive characterization technique for identifying atoms in terms of type and position within a specimen. APT is used to characterize materials in detail and it provides the highest resolution for chemical analysis, which allows studying chemical changes down to nearly atomic resolution. Several common phenomena in materials such as clustering, segregation at grain boundaries and interfaces and phase transformations can be examined. The technique performs better for conducting materials *e.g.* metals, however, it can also be used to study semiconductors, oxides, and even biological materials. The average volume that can be studied is in the range of $50 \times 50 \times 200\ nm^3$. References for this section are [89–91].

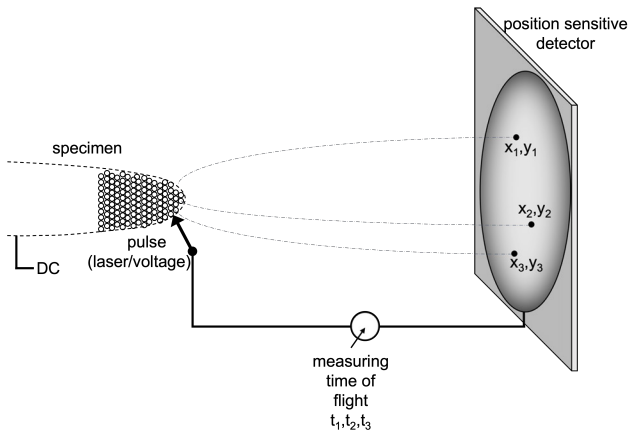

Figure 4.11: Schematic of APT experimental setup.

Figure 4.11 shows the basic principle of APT. A direct current (DC) positive electric field is applied to a needle-shaped specimen with a tip diameter of some tens of nanometers under ultra-high vacuum and at cryogenic temperatures (30–70 K). Since the radius of the tip is small, the field at the surface is very high (several tens of V/nm) and ionized atoms or molecules at the tip surface are evaporated and emitted from the specimen. This process is called *field evaporation*. The penetration depth of the field is very low, and therefore only ions at the surface are evaporated. The evaporated positive ions depart the specimen surface and hit a position sensitive detector, where a highly magnified image of the tip is created. To determine the chemical identity of each ion, the time of flight is measured. The position, time of flight, and sequence of ions can all be used to create a 3D reconstruction of the material being studied. The applied electric field causes high strains in the specimen that sometimes results in failure of the experiment due to specimen fracture.

CHAPTER 5

Experimental details

This chapter describes the details of the experiments, *e.g.* the cutting conditions and workpiece materials, that were used in this study. Additionally, various experimental procedures, such as sample preparation and characterization techniques that were used, are also described here.

5.1 CVD of textured coatings

The focus of this study is on chemically vapor deposited α-alumina coatings. These experimental coatings were deposited both at Sandvik Coromant (Paper I & V) and at Seco Tools (Papers II-IV). α-alumina was deposited as the topmost layer of multilayered coatings. All these coatings were deposited in computer-controlled hot-wall reactors to gain maximum deposition reproducibility. The samples produced at Seco Tools, were loaded on pegs on trays and loaded into a SuCoTec 600HT CVD reactor together with filler and control inserts. The inserts were loaded at the center radius of the tray and in the middle of the stack to get the most even coatings on the surface of the inserts. The multilayered coatings (Figure 2.2) consist of an inner TiN layer deposited at around 930 °C, followed by a medium temperature CVD Ti(C,N) layer deposited at around 885 °C. Then a bonding layer (Ti(C,N,O)) was de-

posited at around 1000 °C followed by an α-Al_2O_3 layer, which was deposited at 1000 °C with different textures of (0001), (01$\bar{1}$2), (11$\bar{2}$0) and (10$\bar{1}$0). These planes are called *c, r, a, m*-planes, respectively, and each texture means that the respective crystallographic plane is deposited normal to the growth direction. Figure 5.1 shows the position of these planes in the α-Al_2O_3 crystal structure. TiN was deposited from the $TiCl_4$-N_2-H_2 system, Ti(C,N) was de-

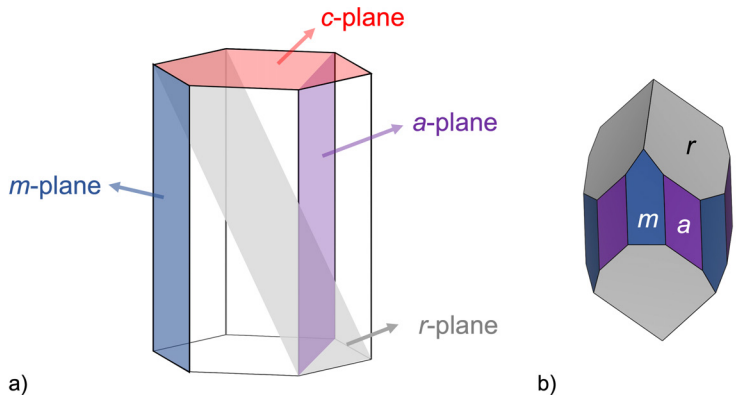

Figure 5.1: (a) Schematic drawing of *c*-plane (0001), *r*-plane (01$\bar{1}$2), *a*-plane (11$\bar{2}$0) and *m*-plane (10$\bar{1}$0) (b) An α-Al_2O_3 crystal composed of {01$\bar{1}$2}, {11$\bar{2}$0} and {10$\bar{1}$0} facets.

posited with medium temperature CVD (MTCVD) using the gas combination $TiCl_4$-CH_3CN-N_2-H_2. The Ti(C,N) layers were oxidized using CO_2/H_2 gases prior to the Al_2O_3 deposition, forming bonding layers. Finally, the alumina coatings were deposited using $AlCl_3$, CO_2 and H_2 gases, where the $AlCl_3$ was generated through the chlorination of Al with HCl.

The Ti(C,N)/α-alumina multi-layer coatings were deposited on inserts of commercial cemented carbide grades with a geometry corresponding to ISO codes CNMG120408-PM (a 80°rhombic insert with 12 mm cutting edges, 4.76 mm thickness and 0.8 mm corner radius). The coated inserts were used for turning experiments. Coatings were also deposited on substrates with a CNMA geometry with planar surfaces in order to allow for more accurate and easier experiments, *e.g.* XRD to be done on as deposited coatings. The shape and some important dimensions and parts *e.g.* rake face, flank face, main and secondary cutting edges of these grades are shown in Figure 5.2.

Ti(C,N) coatings (Paper V) were deposited on cutting tools with a CNMG120408-PM geometry. The CVD depositions were carried out in an industrial scale CVD reactor (Bernex 530 type), with the inserts positioned in the middle of the reactor at the half-radius of the coating tray (middle position). Both (100) and (211) textured Ti(C,N) coatings were deposited onto inner 0.3 µm thick

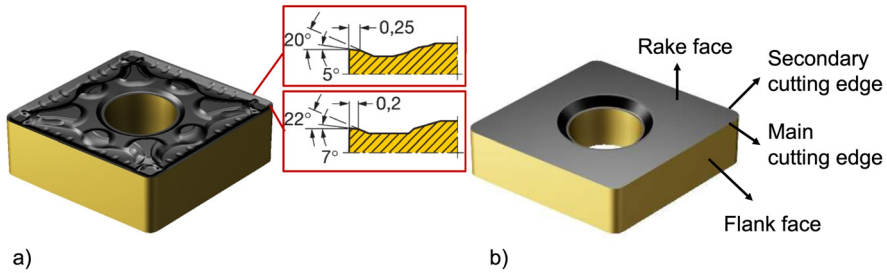

Figure 5.2: Schematic drawing of commercial inserts used as substrates in this work. (a) CNMG geometry and some important dimensions at the nose and cutting edge; (b) CNMA geometry and different parts.(Courtesy of Sandvik Coromant.)

TiN layer at 885 °C. The produced coatings were between 11 and 17 μm thick. For more details, the readers are referred to Paper V.

5.2 Turning tests

In this work longitudinal turning tests were done in order to monitor and measure the wear of the coatings on the inserts. The details of the workpiece material used and the cutting conditions are explained in the following sections.

5.2.1 Workpiece materials

The workpiece material used in the Papers II-V is the 100CrMo7-3 (Ovako825B) steel. The chemical composition of this steel is presented in Table 5.1. The workpiece material is a bearing steel and some of the main mechanical properties of this workpiece material are presented in Table 5.2.

Table 5.1: Chemical composition (in wt.%, balance Fe) of the workpiece material used in the papers

Steel type	C	Si	Mn	Cr	Ni	Mo	Al	O ppm	Ca ppm	S
Ovako825B 100CrMo7-3	0.96	0.26	0.67	1.67	0.15	0.23	0.034	4.5	—	0.007

Table 5.2: Mechanical properties of the workpiece material used in Papers II-V

Steel type	Condition	Yield strength [MPa]	Tensile strength [MPa]	Hardness [HB]
Ovako825B 100CrMo7-3	+SA	460	700 typical	205

5.2.2 Cutting conditions

The machining tests presented in Papers II-IV were performed using a modern CNC lathe. Longitudinal turning tests were done using CNMG120408-PM inserts with three different α-Al_2O_3 and two different Ti(C,N) coating textures. The textures used for turning experiments are (0001), $(01\bar{1}2)$ and $(11\bar{2}0)$ for α-alumina and (100) and (211) for Ti(C,N). All three α-Al_2O_3 coating textures were machined with a cutting speed (v_c) of 220 [m/min], feed rate (f) 0.2 [mm/revolution], depth of cut (a_p) 2 [mm] for 2 minutes and without using coolant. The rake and entering angle were 6° and 95° respectively, which were are a result of the used tool holder. Additionally, the cutting forces were measured using a Kistler device when turning using twin inserts with identical geometry and coating, and using the same workpiece material and cutting conditions. The machining tests for the Ti(C,N) coatings (Paper V) were carried out using the same bearing steel workpiece material (100CrMo7-3) in a modern CNC lathe for (100) and (211)-textured coatings. The samples were machined using longitudinal turning for 1 minute. The cutting speed (v_c) was 220 [m/min], the feed rate (f) was 0.3 [mm/revolution] and the depth of cut (a_p) was 2 [mm]. A water miscible cutting fluid was used as coolant.

For the α-alumina coatings, three inserts of each specific texture, were used for machining tests with a specific cutting condition. One out of three inserts was after each test etched with a warm 35% HCl solution in order to remove any adherent workpiece material. The aim of the turning tests was to monitor and compare the steady-state crater wear of coatings with different textures when machining the same workpiece material. Carefully selected cutting data were employed in order to measure and study the wear of the α-Al_2O_3 layers. For the Ti(C,N) coatings, one insert for each specific texture were used for machining with the given cutting condition. The samples were etched with a warm 35% HCl solution to remove adherent workpiece material after the initial microscopy investigations. The turning test were done to monitor and compare the plastic deformation on the rake face of the inserts.

The turning tests were done in predefined and controlled intervals and all cutting data were carefully monitored and stored. Between each interval, the machine was stopped and the flank tool wear (maximum width of the flank wear land, VB) was measured using a stereo optical microscope. The chips

were also collected for each machining tests if any future studies of the chips should be needed.

5.3 Characterizations

X-ray diffraction

XRD was carried out on the CVD coated cemented carbide inserts. The method was used to check and analyze the coating textures for α-Al_2O_3 and Ti(C,N). The XRD measurements where carried out at Sandvik Coromant and Seco Tools using a Bruker D8 Advance instrument using CuKα radiation. The XRD was used with a Θ-2Θ scan setup. The obtained diffractograms from the XRD measurements, are used to identify the preferred grain orientations of each sample and evaluating the degree of texture by calculating texture coefficients (TCs) using equation 2.4, as described in Chapter 2.

Scanning electron microscopy

In this work a Leo Ultra 55 FEG SEM and an FEI Quanta 200 FEG Environmental SEM (ESEM) were used. Both microscopes were equipped with an Oxford INCA EDX system and in-lens (only Leo Ultra 55) and standard SE detectors. These SEMs were mainly used for imaging of the top surfaces and cross-sections in secondary electron mode, in order to characterize the coating morphology, while the backscattered electron mode was used to mainly identify the adhered workpiece material and inclusions on the coating surface. In order to avoid charging of the α-alumina coatings, either the samples were coated with a thin layer of Pd using a sputter coater or a low accelerating voltage (3 keV) with a working distance of about 5 mm was used. Additionally, these microscopes were used for analyzing the chemical composition of the coatings, especially after machining tests.

X-ray Energy dispersive spectroscopy

XEDS was used in combination with both SEM and TEM. Figure 5.3 shows an example of XEDS performed in SEM on the worn alumina coated inserts. The qualitative XEDS maps, which are maps of elements obtained by preforming XEDS on a region of a specimen, show the presence of the workpiece steel matrix and inclusions, adhering to the insert surface, and the underlying alumina coating.

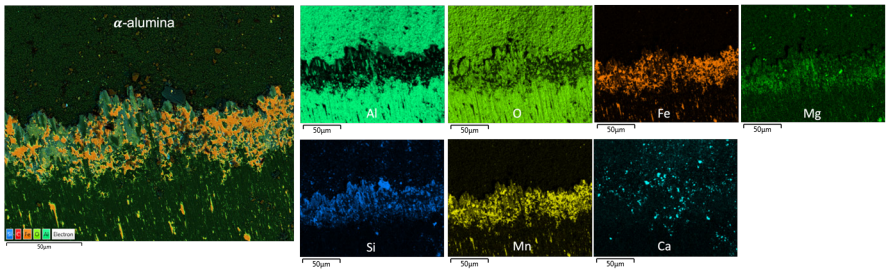

Figure 5.3: XEDS map of the surface of a worn insert coating after turning steel workpiece material. The map shows the main elements of adhered workpiece material on the worn Al_2O_3 coating.

Electron backscatter diffraction and Transmission Kikuchi diffraction

In the present work, EBSD was used for multiple purposes. The main task is to determine the crystallographic orientation of the grains. The obtain data can be used for analysis of texture and assessment of possible plastic deformation by determination of local Schmid factors. The crystallographic orientation of as-deposited α-alumina and Ti(C,N) coatings were examined in top-view. A defect-free surface is important for EBSD. Thus, the results are very sensitive to the method of sample preparation. It was found that mechanical polishing can easily induce strain and damage to the coatings resulting in blurred Kikuchi patterns. In this work EBSD was done on either un-polished samples or on slightly and carefully polished surfaces. The sample is mounted on an SEM stage using a 70° pre-tilted holder and silver paste for mounting the sample to the aluminum stub for avoiding possible mechanical drifts. The data was obtained with both NordlysNano and Symmetry S2 EBSD detectors (Oxford Instruments) using an electron probe step size of 100–200 nm and an accelerating voltage of 20 kV. The working distance was maintained about 10 mm, however it depends on the detector position in the SEM. The mapping time depends on the exposure time for the EBSD camera, step size and the area being mapped.

Post-processing of the acquired EBSD data can be done with either the software associated with the detector being used or free software that provides a variety of texture analysis tools for processing of EBSD data. In this work, HKL Channel 5 software (Oxford Instruments) and MTEX [92], which is a free MATLAB toolbox for texture analysis and interpretation, were used. Different form of maps can be obtained from the raw data. Band contrast maps, which are maps showing the contrast of Kikuchi bands for each pixel, were used to reveal the microstructure of the sample being analyzed even though

the orientations of the pixels are not identified. Pole figures (PFs) and inverse pole figures (IPFs) were used in order to identify the preferred orientation (or texture) of the sample in the analyzed area. A PF is a stereographic projection of the crystallographic plane normals present in the grains. An IPF map is a stereographic projection of the density of all lattice plane normals for a specific sample orientation.

Orientation maps (IPF maps) were used (Papers I-V) to show the crystallographic orientation of each grain with respect to the growth direction. By defining a load angle and direction to the sample, Schmid factor maps (Papers II,IV) for a given slip system can be obtained. The map shows color coded Schmid factor (m) values for each grain. An example of IPF maps and pole figures for two different textures of α-alumina is shown in Figure 5.4, where the three-dimensional orientation of the grains is also visualized on the maps.

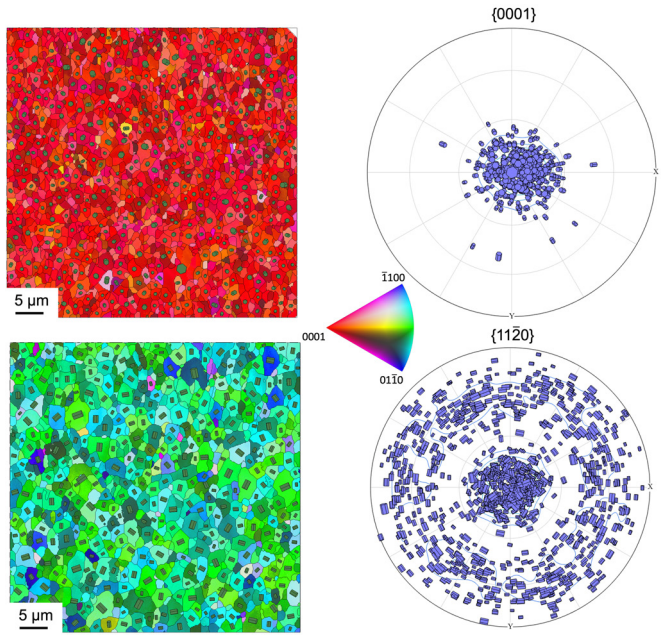

Figure 5.4: IPF maps (left) and pole figures (right) obtained from EBSD on {0001} (top) and {$11\bar{2}0$}-textured (bottom) α-alumina coatings. Three-dimensional shapes of the crystals are visualized on the maps.

The data processing in TKD is similar to that in EBSD, which was described in the previous section. As for EBSD, both the HKL Channel 5 and the MTEX software were used for analysis and post-processing of the acquired TKD data. TKD on coating cross-sections was used for analysis and visualization of the given texture components. Also pole figures (PFs) and inverse

pole figures (IPFs) were created and used. cross-sections has an advantage over plan views in that by knowing crystal orientation of the grains on the cross-section of the coatings makes it also possible to calculate projection of certain crystallographic planes for each grain, which makes it possible to identify different crystallographic facets of the grains. This method was used in Paper IV.

Transmission electron microscopy and Scanning transmission electron microscopy

The TEM instruments used in this work are an FEI Tecnai T20 working at 200 kV and an FEI Titan 80-300 TEM/STEM working at 300 kV, both equipped with a Gatan low background double-tilt specimen holder. The electron sources used was a LaB_6 in FEI Tecnai T20 and FEG in the FEI Titan 80-300 TEM/STEM.

STEM imaging was mainly used to obtain details of the microstructure of the worn and as-deposited coatings. Using STEM and TEM was essential in this work, since the affected region due to wear is in the order of nano-meters. Bright field mode was used to investigate dislocations, to observe the deformed regions and nano-domains close to the surface.STEM HAADF images and XEDS analysis were used to identify different phases, *e.g.* inclusions and pieces of adhered workpiece material on the surface and the observation of heavy elements that diffused from the substrate (Paper I). Figure 5.5 shows BF and HAADF micrographs of a worn α-alumina coating close to the surface, where pieces of workpiece material can be observed in the coating. An FEI Titan 80-300 FEG TEM was used for obtaining detailed microstructural and defect information from the coating/workpiece interface of the worn inserts. The instrument is equipped with an Oxford INCA XEDS detector, which was used to analyze the chemical composition of the microstructural features and products formed on the surface of the worn coatings.

Focused ion beam/scanning electron microscopy

An FEI Versa 3D and an FEI Helios Focused Ion Beam system operating at 30 kV were used to prepare cross-section TEM samples. After the deposition of a protective Pt-layer, the milling of a TEM lamella was initiated with an ion current of 50 nA to cut trenches on either side of the Pt layer, see Figure 5.6a. As the milling progressed, the current was successively reduced. Currents as low as 500 pA were used for the final thinning of the sample. The approximate dimensions of the final sample were 17–20 µm (length) × 5–10 µm (height) × 100–150 nm (thickness). The sample was lifted out from the bulk using an

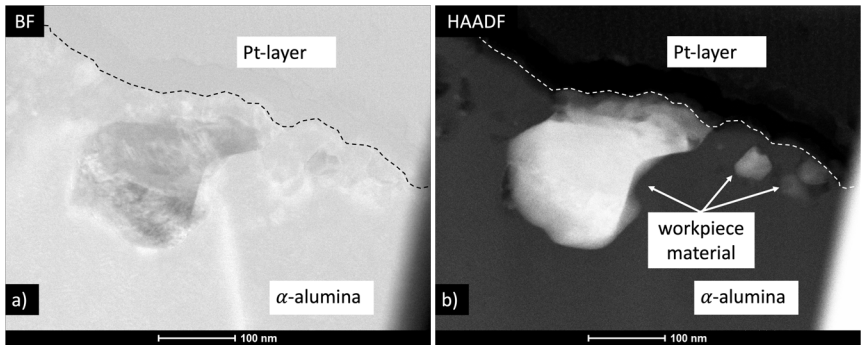

Figure 5.5: STEM BF (a) and HAADF (b) micrographs of a worn α-alumina coating close to the surface. Peices of workpiece material can be observed in the coating. A protective layer of Pt was deposited on the surface to prevent FIB milling damage.

Omniprobe micromanipulator, and with the aid of Pt deposition, and thereafter placed on a Cu grid, as shown in Figure 5.6b, before the final thinning. The final thinning is done by tilting and milling both sides of the lamella with low currents in order to reach the desired thickness suitable for subsequent TEM or TKD investigations.

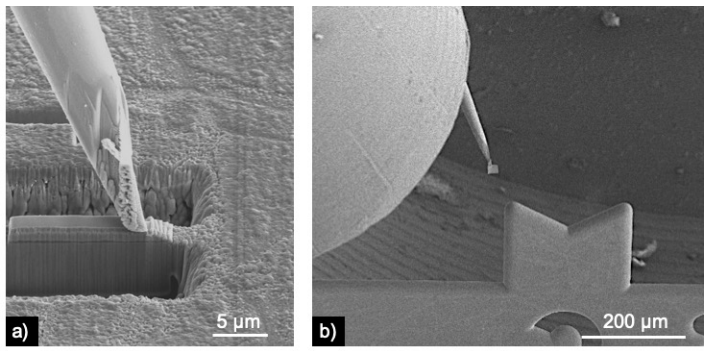

Figure 5.6: Scanning electron micrographs illustrating a FIB-SEM lift-out procedure.

Atom probe tomography

After preparation of the atom probe needles from the interface of the alumina and adhered workpiece material, by implementing a well-known procedure for sample lift-out preparation [90], APT measurements were performed using a LEAP 3000X HR operating in pulsed laser mode with 200 kHz laser pulse frequency, 30 K specimen temperature, 0.3 nJ laser pulse energy and 0.20%

evaporation rate. For data reconstruction and evaluation CAMECA IVAS 3.6.14 software was used. A proximity-histogram was calculated starting from a 40 at.% O iso-surface, using 0.05 nm steps, 1 nm^3 voxel size and $3 \times 3 \times 1.5$ nm^3 delocalization distance across the interface.

CHAPTER 6

Results and discussions

6.1 Summary of results

For this thesis work, several different textures of α-alumina coatings were synthesized using CVD. The microstructure and texture of as-deposited and worn CVD α-alumina coatings were studied. In the first paper, texture development as a function of height in the coating for (0001) and $(10\bar{2}0)$ textures was investigated by studying the microstructure of three different CVD α-Al_2O_3 layers when deposited onto a Ti(C,N,O) bonding layer. The effect of catalyzing gas on texture development of (0001)-textured coatings as well as diffusion of heavy elements from the substrate through the coatings were investigated. In the second paper, the effect of coating texture on the wear of the coatings was investigated through Schmid factor analysis. In the third paper, the effect of coating texture on the wear of the coatings was investigated by analyzing the surface morphologies in detail on the rake face and the initiation of crater wear. In the fourth paper, a thorough study was performed on some important features seen on the worn surfaces. The fifth paper, concerns the ability of plastic deformation in Ti(C,N) with two different textures using the method developed in Paper II for studying the Schmid factor. The major findings of these studies will be briefly discussed in the following sections. The reader is referred to the appended papers for further detailed results.

6.2 As-deposited textured alumina coatings

The interfacial microstructure and texture development were investigated in three textured CVD α-alumina coatings (Paper I). The α-alumina layers were deposited on a Ti(C,N,O) bonding layer, on top of a TiN-Ti(C,N) layer. The multilayered coatings were deposited onto cemented carbide/cobalt substrates (WC-Co).

By using STEM and XEDS it was observed that grain boundary diffusion of W and Co occurred through the TiN and Ti(C,N) layers to the bonding layer/α-alumina interface. This can be the source of observed defects at the bonding layer/α-alumina interface, as well as the disturbance of nucleation and early growth of the alumina layer. It was also shown that when H_2S was introduced as a catalyzing gas during the nucleation step, more voids were formed, while the number of voids were similar when H_2S was not used during the initial deposition step of (0001)- and $(10\bar{1}0)$-textured coatings. It seems possible that these voids are due to high reactivity of H_2S gas that etches the specimen surface when initially introduced to the reactor. Grain boundary diffusion of heavy elements from the substrate to the Ti(C,N,O) bonding layer and the α-alumina interface, as well as the observed voids at the interface, are shown in the STEM HAADF micrographs in Figures 6.1a and b, respectively.

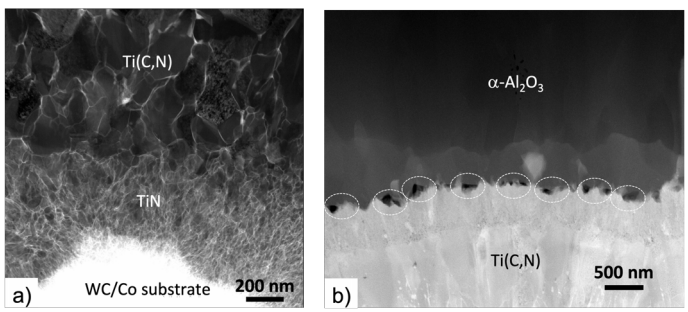

Figure 6.1: STEM HAADF micrographs showing (a) grain boundary diffusion of heavy elements from the substrate towards the bonding/α-alumina interface in Sample (001) ((0001) texture) and (b) the observed voids at the alumina/bonding layer interface when catalyzing gas is introduced during (0001)-textured α-alumina deposition (Sample (001)+). Reproduced from Paper I.

The morphology of the alumina grains developed from equiaxed grains at the bottom of the alumina coating to columnar grains at the top. The size of the grains also increased significantly from ≈100 nm at the bottom to several microns at the top. By performing TKD on the alumina coating cross-sections, it was revealed that small equiaxed grains at the inner part of the alumina coatings had a more random orientation. The orientation of the grains in the

coating developed to the desired texture, both as a gradual change over several grains and as an abrupt transformation from one grain to another. Additionally, it was observed that the presence of H_2S gas decreases the number and thickness of small equiaxed grains with non-preferred orientations as shown in Figure 6.2 and thus, H_2S gas promotes an earlier development of the (0001) texture, and also results in more voids at the bonding layer/alumina coating interface.

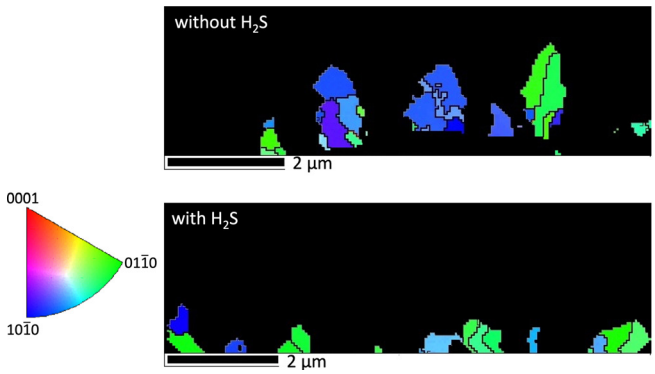

Figure 6.2: IPF maps showing small grains with non-preferred orientations (c-axis is tilted 70–90° away from the surface normal) for (0001) texture when H_2S gas was not present and when H_2S gas was introduced during the nucleation step. Reproduced from Paper I.

6.3 Facet analysis

By knowing the crystallographic orientations of the grains, it is possible to analyze and identify the created facets on the as-deposited α-alumina coatings. This method was developed and described in detail in Paper IV. The surface shapes of the coating grains can be seen in the SEM plan-view image of (0001)-textured α-alumina coating in Figure 6.3a The grains have various shapes, such as pyramidal with three or more sides. Cross-sections of the α-alumina layer shows that the majority of the facets are pyramidal, although other facets (basal and prismatic) are also present. The grains either have two pyramidal facets or multiple facets composed of distinct prismatic, basal and pyramidal facets. Around 67 percent of the facets were pyramidal facets, 22 percent were prismatic facets and 11 percent were basal facets. It should be noted that depending on the exact position of the lift-out specimen with respect to the grains at the surface of the sample, different facets will be seen in cross-section images (such as Figure 6.3a).

The surface morphology of the grains and their facets, as well as the cross-

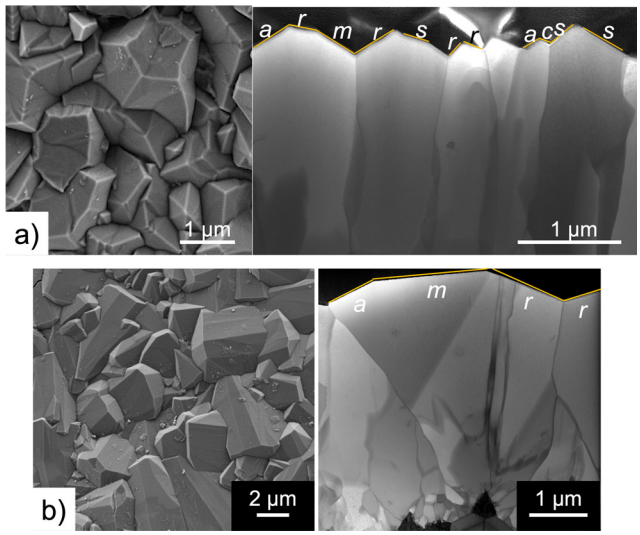

Figure 6.3: SEM plan-view image (right) and STEM BF image (left) of the as-deposited CVD α-alumina layer showing the typical surface morphology and type of the facets in (a) (0001)-textured and (b) $(11\bar{2}0)$-textured coatings. Reproduced from Paper IV

section of the $(11\bar{2}0)$-textured α-alumina coating, are shown in Figure 6.3b. The facets in this sample are either prismatic or pyramidal because the c-axes of the grains are lying down, but the facets still come in a variety of shapes with varied and complex structures. As seen in Figure 6.3b, the facets are quite big, with a size of more than 1 μm. This is much larger than the facets of as-deposited (0001)-textured coatings, which are 500 nm or less in length. This is related to the significantly larger grain size of the $(11\bar{2}0)$-textured coating. The angles between the facets for this texture are larger, which is related to the texture (normal direction) in relation to the formed facets. Measuring all the facets in the whole thin-foil specimen of the as-deposited $(11\bar{2}0)$-textured coating reveals that there is an almost equal number of pyramidal and prismatic planes.

6.4 Schmid factor analysis

A thorough analysis of the Schmid factors (m) for three different (basal and two prismatic) slip systems, and three different coating textures (0001), $(01\bar{1}2)$ and $(11\bar{2}0)$ was performed in Paper II. This was done in order to understand the influence of a CVD α-alumina coating texture on the ability of the coating to deform plastically at different locations on the rake face of a cutting tool

insert during a metal cutting operation. The results obtained for the ideal textures were compared with the three experimental CVD coatings. The results for differently textured coatings were compared and related to the observed deformation behavior.

Schmid factor diagrams were constructed using MATLAB/MTEX and used to extract frequency distributions for different slip systems and textures, both in ideal cases (theoretically) and for CVD grown coatings. The results were compared with lateral distribution maps of Schmid factors obtained from experimental coatings using electron backscatter diffraction. Using SEM, the microstructure and surface topography of the worn alumina layers in different wear zones (see Figure 3.7) were investigated. It was found that there is an association between the ridge-shaped, elongated, surface features and higher wear rates in the transition zone. A flatter surface morphology and a higher probability of discrete plastic deformation are connected to less wear.

It was also observed that basal slip is most easily activated in the transition zone at the highest temperatures and external forces, followed by prismatic slip systems 1 and 2, in the (0001)-textured coating. The homogeneous plastic deformation behavior of the coating with (0001) texture is also connected to the concentration of m-values toward the highest m. The other two coatings contained some grains with very low Schmid factors, and these grains didn't deform as other grains with high Schmid factors. The differences in the m-value distribution between the three slip systems are not large for the $(01\bar{1}2)$ and $(11\bar{2}0)$ textured coatings, and the m-value distributions are relatively wide. The correlation of theoretical and experimental m-values for the basal slip system to the obtained surface morphology and the resulting wear rates are shown in Figure 6.4 for (0001)- and $(11\bar{2}0)$-textured coatings with differences. As previously stated, there are strong links between high m-values with low spread to flatter surface morphology and large spread of m-values to the ridge-shaped, elongated, surface features.

The Schmid factors are low for all slip systems in the sticking zone of the (0001) textured coating. In the $(01\bar{1}2)$ textured coating, basal slip is most easily activated, followed by prismatic slip 1 and 2. The $(11\bar{2}0)$ textured coating shows different results in this zone, as the prismatic slip system 2 exhibits high m-values, while prismatic slip 1 shows intermediate values and basal slip low values.

It is clear that the Schmid factor analysis forms an important basis for understanding crater wear, especially when it is connected to local plastic deformation of textured CVD α-Al_2O_3 coatings. The methodology of this work have been expanded to other coating systems (titanium carbonitride in Paper V) where it is of interest to analyze the deformation behavior and local plastic anisotropy of different textures, see section 6.6.

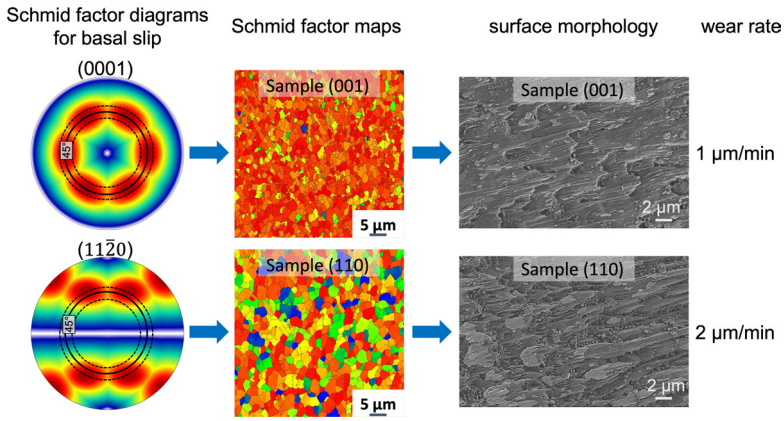

Figure 6.4: Schematic illustration showing the correlation between the theoretical, experimental Schmid factor analysis for basal slip system to the resulted surface morphology in the transition zone and the wear rate for the two (0001) and (11$\bar{2}$0)-textured alumina coatings.

6.5 Wear of α-alumina

The results presented here give a better understanding of the effect of texture on the wear of α-alumina coatings and the underlying wear mechanisms for these coatings. These results were obtained from both the surface, on a larger scale, and more detailed cross-sectional studies of the specific features observed on the surface.

6.5.1 Overview wear and surface morphology

The surface morphology and microstructure of worn coatings on the crater wear were investigated in three textured CVD α-alumina coatings in Paper III. The surface morphology, amount of adhered workpiece material and thickness profiles of the worn coatings were compared and linked to the texture of the coatings. In addition, the surface roughness of the chips and applied tangential and feed forces during cutting were measured and compared.

It was noted that different mechanisms are responsible for the wear of different coating textures and in different zones (see Figure 3.7). It was observed that in the sticking zone, due to the low flow of the workpiece material and high temperatures that are generated by the deformation of the workpiece material, due to very large compressive forces, chemical reactions might be induced between the soft and hot workpiece material and the α-alumina coating, causing a chemical etching effect. This etching effect exposes low energy facets on the

grain asperities forming so-called terraces. These terraces were observed on all coatings with three different textures ((0001), $(01\bar{1}2)$ and $(11\bar{2}0)$). However, they were parallel to the surface on (0001) texture and were inclined in the other two textures. This was believed to be related to the crystal orientation of the grains and particularly the basal planes of α-alumina, since these are parallel to the surface in (0001)-textured coatings and are inclined in $(01\bar{1}2)$ and $(11\bar{2}0)$-textured coatings. In this zone, ductile fracture of some of the grains in $(01\bar{1}2)$ and $(11\bar{2}0)$-textured coatings were observed, which can be a result of lateral rotation of the fiber-textured grains. A large number of small and hard particles on the surface were indications of fracture of these two coatings. The wear thickness profile didn't show any significant wear in this zone for all the three textured coatings. However, rougher surfaces were created as a result of ductile fracture and formation of ruptured-like regions on $(01\bar{1}2)$ and $(11\bar{2}0)$-textured coatings, especially for the $(11\bar{2}0)$-textured coating, which had a larger grain size.

In the transition zone, especially at the end closer to zone III, more severe wear and plastic deformation were observed. The surface morphology was very flat and smooth for the (0001)-textured coating, while the surface consisted of elongated ridges in the coatings with $(01\bar{1}2)$ and $(11\bar{2}0)$ textures. This implies that the main wear mechanism in this zone is plastic deformation. The smooth and flat surface developed on (0001)-textured coatings is probably the result of a homogeneous basal slip type of deformation, while only some grains in $(01\bar{1}2)$ and $(11\bar{2}0)$-textured coatings plastically deform, shaping the elongated ridges. The surface morphology variations in (0001) and $(11\bar{2}0)$-textured coatings can be observed in Figure 6.5.

Plastic deformation of these grains is also connected to the high Schmid factor values of different slip systems for these grains. The heterogeneous surface morphology observed on $(01\bar{1}2)$- and $(11\bar{2}0)$-textured coatings could be linked to the heterogeneous distribution of Schmid factor values for these textures. The coating debris created in the neighboring zone can also cause abrasion in the $(01\bar{1}2)$- and $(11\bar{2}0)$-textured coatings. However, it seems that this effect of abrasion and also of grain size is marginal in the total wear since these two coatings had different grain sizes, and different amounts of particles were observed on the surfaces, while the wear rates were similar.

In the sliding zone, the surface morphology in the previous zone is further developed due to the flow of workpiece material. The smooth and flat surface of the (0001)–textured coating results in the creation of a shallow crater and a low wear rate. The deeper wear craters and higher wear rates of the $(01\bar{1}2)$- and $(11\bar{2}0)$–textured coatings are connected to the heterogeneous plastic deformation and associated abrasion of their rougher surfaces. The results imply that the impact of coating texture on the relevant wear mechanisms and the amount of wear is significant. It seems that grain size does not influence the

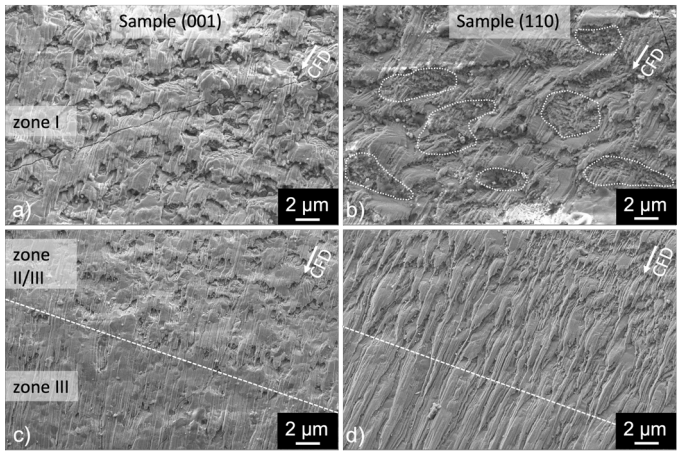

Figure 6.5: SEM micrographs of the transition and sliding zones of Samples (001) and (110) tilted 45°. The micrographs show (a-b) the sticking zone (zone I) with ruptured-like areas marked and (c-d) the boundary region between the transition and sliding zones (zone II/III). The adhered workpiece material was removed by chemical etching. The chip flow direction (CFD) is indicated. Taken from Paper III.

wear rate significantly during the cutting conditions used, however, it results in forming a coarser surface morphology.

The outcome of the performed investigation is that the mechanical response of the three various textured coatings is very different. All textures undergo plastic deformation, while $(01\bar{1}2)$ and $(11\bar{2}0)$ textures also undergo ductile fracture of individual grains. (0001) texture develops a smooth wear surface affected by basal glide. In contrast to previously published articles, there was no significant scratching or abrasive wear from non-metallic inclusions in the steel.

6.5.2 Cross-sectional studies: facet identification, surface chemistry and plastic deformation

The effect of alumina coating texture on the wear mechanisms in different wear zones on the insert rake face was investigated in detail. This was evaluated in dry turning of a bearing steel workpiece material for two textured coatings, (0001) and $(11\bar{2}0)$. The developed surface and sub-surface features were linked to the orientation of individual grains, thereby creating a fundamental understanding of the active wear mechanisms and machining performance.

It was observed that the degradation of the worn coatings starts from the edge of the inserts with terrace formation, probably due to crystallographic dependent etching. The terraces consist of steps of c- and r-facets, with heights of 30–60 nm, Figure 6.6a, forming horizontal surfaces in (0001)-textured alumina, see Figure 6.6b. The terrace formation in $(11\bar{2}0)$-textured alumina is highly influenced by the fiber-texture. Tilted terraces form in grains with basal planes parallel to the chip flow direction, while no terraces form when the basal planes are perpendicular to the chip flow direction, see Figure 6.7.

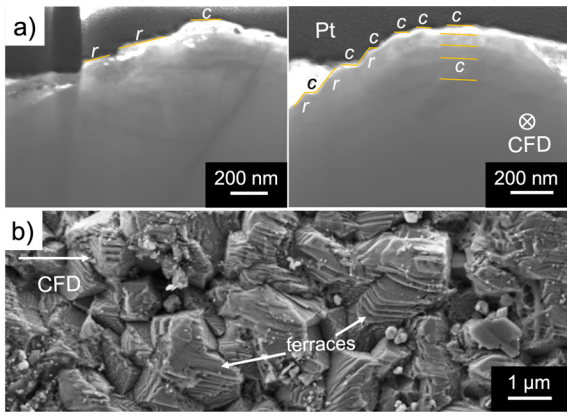

Figure 6.6: (a) STEM BF image showing a terraced grain in higher magnifications. Some small, identified facets are marked. (b) SEM secondary electron plan-view micrograph of the surface morphology of the alumina grains close to the edge of (0001)-textured alumina after machining. Some terraces are marked with arrows. Reproduced from Paper IV.

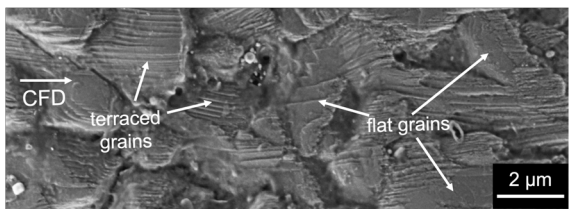

Figure 6.7: SEM secondary electron micrograph of the surface morphology of the alumina grains at the edge of the insert for $(11\bar{2}0)$-textured alumina after machining. Grains with flat surfaces, grains with inclined terraces, as well as the CFD are marked. Reproduced from Paper IV.

Larger c-facets are frequently created for grains in the sticking zone of the (0001)-textured coating when the m-planes are perpendicular to the chip flow direction. Otherwise, the grains exhibit a rounded surface. The $(11\bar{2}0)$-textured alumina exhibit grains with one large or several small a-facets when the basal planes are perpendicular to the chip flow direction; if they instead are

parallel, a complex, deformed surface with a ruptured-like, rough morphology develops, see Figures 6.8a and b for deformed and faceted grains respectively.

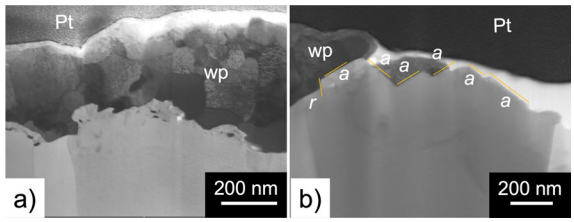

Figure 6.8: STEM BF micrograph of the cross-section of $(11\bar{2}0)$-textured alumina layer in zone I where (a) a deformed grain and (b) a faceted grain are shown. Small facets are identified and marked in the image. Cross-sections are perpendicular to the CFD. Reproduced from Paper IV.

More deformation occurs for both the textured coatings in the transition zone, with an associated sub-surface dislocation formation. A wavy pattern with some microns spacing is created, with steps present at larger misalignments of the lattice planes in neighboring grains. Figure 6.9 shows this type of misalignment causing steps in the (0001)-textured coating.

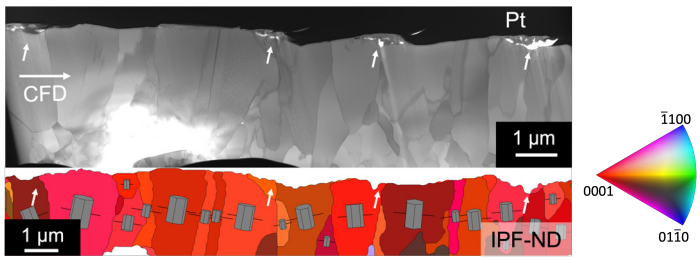

Figure 6.9: (top) STEM BF micrograph showing the cross-section of the (0001)-textured alumina layer parallel to the CFD (etched). (bottom) IPF map in the coating normal direction (ND) of the same cross-section. Hexagonal crystals, as well as c-intersection lines for each grain, are added to the IPF map. Locations of steps are marked with arrows in the micrograph and the IPF map. Color key to the IPF map is shown. Reproduced from Paper IV.

The spacing between the steps is shorter in the $(11\bar{2}0)$-textured alumina, which is linked to more frequent and larger misalignment of the lattices in neighboring grains, due to the fiber texture resulting in grain rotations around $(11\bar{2}0)$. Some stepped grains (c-facets for (0001) texture and a-facets for $(11\bar{2}0)$) texture are still visible in this zone. A significantly rougher surface was developed in the $(11\bar{2}0)$-textured coating, as a result of heavy plastic deformation of the grains with basal planes parallel to the chip flow direction, leading to ridge formation.

The development of the surface morphologies is coupled to the number of activated slip systems. It was observed that if only one of the major slip systems (basal, prismatic, pyramidal) is activated flat facets are developed, while if several slip systems are activated ridges are instead formed.

The surface morphology in the sliding zone is mainly affected by the surface developed in the previous zones. No connection between the surface morphology and orientation of individual grains is found in this zone. The developed surface is smooth for the (0001) texture and significantly rougher for the $(11\bar{2}0)$ texture. The larger number of small round coating fragments in the sliding zone of the $(11\bar{2}0)$ texture is related to the larger degradation of this coating. The difference in surface roughness can be seen in Figures 6.10a and b, which show the plan-view surface morphology and their cross-sections perpendicular to the chip flow direction for (0001)- and $(11\bar{2}0)$-textured alumina, respectively.

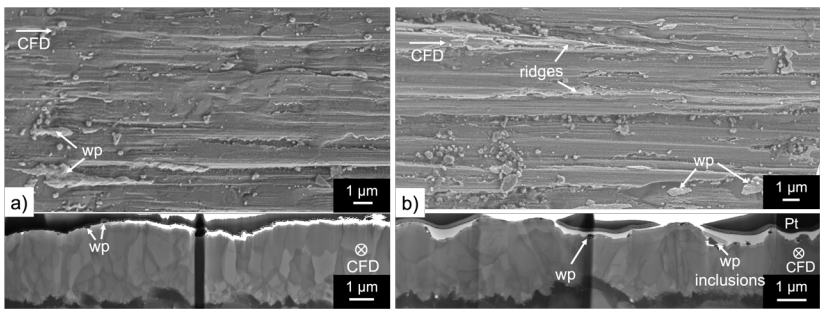

Figure 6.10: SEM secondary electron micrograph of the surface morphology (top) and STEM BF micrograph showing the cross-section (bottom) of the alumina layer in the sliding zone for (a) (0001) texture and (b) $(11\bar{2}0)$ texture. Some features in the figures are indicated with arrows. Chip flow direction (CFD) is marked in the figures. Reproduced from Paper IV.

The chemical reactions between the alumina layer and the workpiece material are found to be limited, and results of atom probe tomography show that basically no intermixing between the alumina and workpiece material is observed. This study reveals the complex relationships between local wear mechanisms and coating texture. This fundamental understanding can facilitate future development of texture-controlled CVD α-alumina coatings, with the potential of further improving the performance of coated cutting tools.

6.6 Schmid factor analysis for Ti(C,N)

With the method developed in Paper II, it is possible to analyze the influence of the crystallographic texture of the other coatings on their wear by plastic deformation due to the chip flow during machining. This method was applied

on polycrystalline fiber-textured titanium carbonitride coatings with rock salt structure to analyze the ability of these coatings to undergo plastic deformation. The Schmid factors were calculated for coatings with (100) and (211) growth textures, and $\{100\}< 1\bar{1}0 >$, $\{110\}< 1\bar{1}0 >$ and $\{111\}< 1\bar{1}0 >$ as possible slip systems and were related to the observed surface morphology of the two growth textures. The surface morphology was investigated in different areas of the contact zone after adherent workpiece material was removed by warm HCl etching. The results show that the (100)-textured Ti(C,N) coating exhibits more plastic deformation in the sticking zone (zone I) and less plastic deformation at the end of transition and beginning of sliding zone (zone II/III) than the (211)-textured Ti(C,N) coating. The surface morphology of the two textured coatings exhibits signs of plastic deformation in the transition zone, however, a homogeneous deformation occur for the (100) texture in zone (II/III), while it is more heterogeneous for the (211) texture. Surface morphologies of the worn coatings are shown in Figure 6.11.

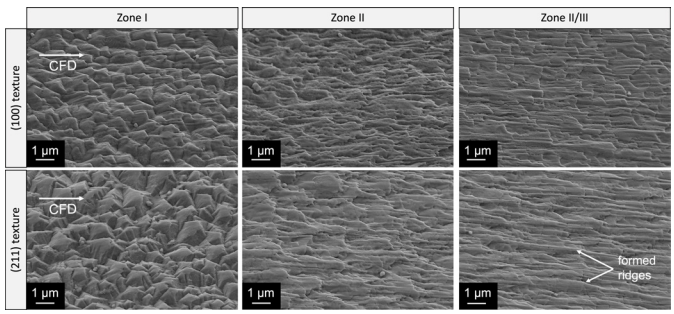

Figure 6.11: SEM micrographs of the Ti(C,N) coatings on the worn rake face of the cutting tool inserts for (100) and (211) textures in zone I, II and II/III, respectively. Ridges formed due to large plastic deformation in (211) texture are marked. Chip flow direction (CFD) is marked in the figures. Reproduced from Paper V.

Analyzing Schmid factors reveals that the observed differences of the surface morphology of the two textured Ti(C,N) are not significantly influenced by $\{111\}< 1\bar{1}0 >$ slips system. The reason is that the Schmid factor diagram obtained for this slip system shows high symmetry for both (100) and (211) textures, resulting in similar deformation for both textures. However, more differences can be observed on the simulated Schmid factor diagrams for $\{100\}< 1\bar{1}0 >$, $\{110\}< 1\bar{1}0 >$ slip systems implying that (100) and (211)-textured coatings are influenced more by these two slip systems. More detailed investigations of these two slip systems and linking them to the observed surface morphology and grain deformation of the worn textured Ti(C,N) coatings on the rake face reveal that the observed differences in surface morphology coincide best with the simulation results of the $\{110\}< 1\bar{1}0 >$ slip systems. Therefore, it is believed that this slip system is the dominant activated slip systems during the metal machining tests applied in this work.

CHAPTER 7

Outlook

The overall aim of this project is to understand the microstructure and wear mechanisms of textured CVD α-alumina coatings. In this thesis, the essential parameters for preparing high-quality TEM lamellae used for both TKD and TEM studies were optimized, as well as TKD parameters, in order to be able to perform a high-quality analysis on coating cross-sections with a high spatial resolution. This made it possible to perform TKD analysis on cross-sections of both as-deposited and worn CVD α-alumina coatings. In this thesis, the microstructure and texture of the as-deposited coatings were studied as a function of height. In addition, a thorough Schmid factor analysis on the textured coatings with different textures were performed and related to experimental data. The wear study of both the surface and cross-sections of the coatings on the rake face of the tool has built a platform that can be used in future studies for obtaining a better understanding of the wear behavior of textured CVD coatings and developing new enhanced coatings.

7.1 Future work

There are numerous phenomena to examine in the never-ending effort of improving our understanding of wear behavior of CVD alumina coated cutting

tools. Three distinct primary, secondary and tertiary shear regions are defined in the machining operations where high temperature and strain locally develop at extreme rates. The focus of this thesis has been the wear on the tool side of the tool-chip contact in the secondary shear zone of the workpiece material. In the future also the tool side of the contact in the primary shear zone where fast shearing metal volumes from the workpiece during chip formation and tertiary shear zone where plastic deformation in the newly machined workpiece occurs due to contact with the tool flank should also be investigated. This approach of wear analysis should also be extended to other hard coatings used in metal cuttings, such as CVD TiAlN and Ti(C,N), as well as other machining conditions, such as using coolant or slow machining. The information gathered under broader criteria allows a better understanding of the wear behavior of hard coatings utilized in cutting tools.

Regarding the chemistry of the coating surface, more in-depth investigations should be performed in order to determine the possible chemical reactions with the workpiece and possible developed phases at different regions of the coatings. This can be done at the interface between the adhered workpiece material and coating or in the region where alumina nanodomains exists using atom probe tomography.

With regard to relating the obtained surface morphology of the grains after machining to the orientation of the grains, three-dimensional EBSD can be performed on a larger volume in order to obtain more statistics.

In addition, nano-sized hard X-ray beams at large-scale facilities can also be used in order to study aspects of the microstructure that help understanding the wear, *e.g.* in-situ X-rays analysis of the coatings during machining or understanding the mechanical properties of differently textured coatings, *e.g.* residual stress and strain. The nano-sized hard X-ray beam at Petra III has been used on tool inserts before and after blasting under different blasting conditions in order to investigate the mechanical properties of the three different textured coatings and to measure the stress in the coatings as a function of coating height, thereby obtaining a better understanding of the residual stresses in these type of coatings, which later can be linked to a better understanding of the deformation mechanisms.

Acknowledgements

To begin, I would like to express my deepest gratitude to Prof. Mats Halvarsson, my main supervisor. He has been a supervisor, a mentor and a friend who has supported me achieving high-quality work while also listening to my problems and advising me on my personal growth during the years of my Ph.D. study. Working with him was really fun and fruitful.

In addition, I would like to deeply and warmly thank Prof. Susanne Norgren, my co-supervisor at Sandvik Coromant, for always believing in me and encouraging me to perform my best. I have always felt like she was someone I could rely on for support. Her level of attention and discipline has always inspired me, and I am very pleased and excited that I can still work with her at Sandvik Coromant and learn from her broad knowledge and expertise. Prof. Hans-Olof Andrén, my co-supervisor, is sincerely acknowledged for his tremendous support of my Ph.D. study. It has been a great pleasure and honor to be one of his students and learn from him. His commitment to research and passion for it has always been inspirational. Prof. Magnus Hörnqvist Colliander, my co-supervisor, is likewise acknowledged for his time and assistance. His passion and his way of working, managing many tasks and projects have fascinated me. I look forward to collaborating and learning more from him in the future.

Chalmers Material Analysis Laboratory is acknowledged for their great support and care of the microscopes and equipment. I would like to also thank all my colleagues and friends from my division, Microstructure Physics and members of Eva Olsson's group for all the activities we had together and for creating a pleasant environment. Special thanks to Dr. Olof Bäcke and Dr. Anand H.S. Iyer who generously assisted me whenever I needed support. Prof. Mattias Thuvander is acknowledged for being generous and flexible with the APT experiments. I am thankful to my examiner, Prof. Lena Falk, for giving me feedback to accomplish my work efficiently. Ola Löfgren is acknowledged for the Macbook and software related issues. My office-mate and friend Dr. Nitesh Raj Jaladurgam, thank you for the fun times and for the life- and science-related discussions we had.

There have been many people at Sandvik Coromant who have assisted me and contributed to the work contained in this thesis in various ways. I would like to express my gratitude to all of you, since it is impossible to mention everyone. Special thanks to my manager Dr. Emmanuelle Göthelid for her prompt support, being flexible and observant of my work-load and assisting me to better integrate and have a smooth transition from Chalmers to the company. Dr. Jan Engqvist and Dr. Linus von Fieandt and all colleagues at CVD Division are acknowledges for their great contributions and support of my Ph.D. study. Dr. Ernesto Coronel, Dr. Mikaela Gustafsson and Dr. Mikael Kritikos and

all colleagues at the Division of Materials Characterization are acknowledged for their support whenever I needed to use the instruments. Ulrika Medin is acknowledged for reading the thesis and the papers and approving their publication.

Seco Tools is acknowledged with special thanks to Dr. Rachid M'Saoubi, Dr. Oscar Alm, and Dr. Tommy Larsson, for their support and contribution to this project.

I would like to dedicate this work to my parents, without whom I would not have achieved anything. Thank you for your unending love and support. Siavash, thanks for being such a nice and supportive brother. I had a lot of fun these years in Gothenburg. Last but not least, thank you, Romy, for being you and for supporting me when I go through tough moments.

Bibliography

[1] Sandvik Coromant (Firm). *Modern metal cutting: a practical handbook*. Sandvik Coromant, 1994.

[2] Understanding cemented carbide. http://www.destinytool.com/carbide-substrate.html. *Accessed 2020-06-10*.

[3] M. Halvarsson. *The microstructure and stability of CVD aluminia coatings*. Chalmers University of Technology, 1994.

[4] B. M. Kramer and N. P. Suh. Tool wear by solution: A quantitative understanding. *Journal of Engineering for Industry*, 102(4):303–309, 11 1980.

[5] B. Lux, C. Colombier, H. Altena, and K. Stjernberg. Preparation of alumina coatings by chemical vapour deposition. *Thin Solid Films*, 138(1):49–64, 1986.

[6] A. Larsson, M. Halvarsson, and S. Vuorinen. Microstructural investigation of as-deposited and heat-treated CVD Al_2O_3. *Surface and Coatings Technology*, 94:76–81, 1997.

[7] M. Halvarsson and S. Vuorinen. Epitaxy in multilayer coatings of κ-Al_2O_3. *Surface and Coatings Technology*, 80(1-2):80–88, 1996.

[8] S. Vuorinen, R. Sakari, and L. Karlsson. Phase transformation in chemically vapour-deposited κ-alumina. *Thin Solid Films*, 214(2):132–143, 1992.

[9] M. Halvarsson and S. Vuorinen. The influence of the nucleation surface on the growth of CVD α-Al_2O_3 and κ-Al_2O_3. *Surface and Coatings Technology*, 76:287–296, 1995.

[10] S. Ruppi. Advances in chemically vapour deposited wear resistant coatings. *Le Journal de Physique IV*, 11(PR3):Pr3–847, 2001.

[11] S. Ruppi. Deposition, microstructure and properties of texture-controlled CVD α-Al_2O_3 coatings. *International Journal of Refractory Metals and Hard Materials*, 23(4-6):306–316, 2005.

[12] S. Ruppi. Enhanced performance of α-Al_2O_3 coatings by control of crystal orientation. *Surface and Coatings Technology*, 202(17):4257–4269, 2008.

[13] R. M'saoubi and S. Ruppi. Wear and thermal behaviour of CVD α-Al_2O_3 and MTCVD Ti (C, N) coatings during machining. *CIRP annals*, 58(1):57–60, 2009.

[14] P. A. Dearnley. Rake and flank wear mechanisms of coated cemented carbides. *Surface Engineering*, 1(1):43–58, 1985.

[15] G Brandt. Flank and crater wear mechanisms of alumina-based cutting tools when machining steel. *Wear*, 112(1):39–56, 1986.

[16] S Ruppi and MTEM Halvarsson. Tem investigation of wear mechanisms during metal machining. *Thin Solid Films*, 353(1-2):182–188, 1999.

[17] J Barry and G Byrne. Cutting tool wear in the machining of hardened steels: Part I: Alumina/TiC cutting tool wear. *Wear*, 247(2):139–151, 2001.

[18] A Osada, E Nakamura, H Homma, T Hayahi, and T Oshika. Wear mechanism of thermally transformed CVD Al_2O_3 layer. *International Journal of Refractory Metals and Hard Materials*, 24(5):387–391, 2006.

[19] Roland Bejjani, M Collin, Thomas Thersleff, and S Odelros. Multi-scale study of initial tool wear on textured alumina coating, and the effect of inclusions in low-alloyed steel. *Tribology International*, 100:204–212, 2016.

[20] R M'Saoubi, O Alm, JM Andersson, H Engström, T Larsson, MP Johansson-Jõesaar, and M Schwind. Microstructure and wear mechanisms of texture-controlled CVD α-Al_2O_3 coatings. *Wear*, 376:1766–1778, 2017.

[21] Martina Gassner, Nina Schalk, Michael Tkadletz, Markus Pohler, Christoph Czettl, and Christian Mitterer. Influence of cutting speed and workpiece material on the wear mechanisms of CVD TiCN/α-Al_2O_3 coated cutting inserts during turning. *Wear*, 398:90–98, 2018.

[22] Axel Bjerke, Andrii Hrechuk, Filip Lenrick, Rachid M'Saoubi, Henrik Larsson, Andreas Markström, Thomas Björk, Susanne Norgren, Jan-Eric Ståhl, and Volodymyr Bushlya. Onset of the degradation of CVD α-Al_2O_3 coating during turning of Ca-treated steels. *Wear*, page 203785, 2021.

[23] GKL Goh, LC Lim, M Rahman, and SC Lim. Transitions in wear mechanisms of alumina cutting tools. *Wear*, 201(1-2):199–208, 1996.

[24] A Larsson and S Ruppi. Structure and composition of built-up layers on coated tools during turning of Ca-treated steel. *Materials Science and Engineering: A*, 313(1-2):160–169, 2001.

[25] S. Ruppi, A. Larsson, and A. Flink. Nanoindentation hardness, texture and microstructure of α-Al_2O_3 and κ-Al_2O_3 coatings. *Thin Solid Films*, 516(18):5959–5966, 2008.

[26] Siamak Shoja. *Microstructure and Plastic Deformation of Textured CVD Alumina Coatings*. Licentiate thesis, Department of Physics, Chalmers Univer-sity of Technology, 2020.

[27] J. O. Carlsson. Processes in interfacial zones during chemical vapour deposition: aspects of kinetics, mechanisms, adhesion and substrate atom transport. *Thin solid films*, 130(3-4):261–282, 1985.

[28] J. E. Sundgren and H. T. G. Hentzell. A review of the present state of art in hard coatings grown from the vapor phase. *Journal of Vacuum Science and Technology A: Vacuum, Surfaces, and Films*, 4(5):2259–2279, 1986.

[29] B. Lux, R. Haubner, and C. Wohlrab. Chemically vapour-deposited hard coatings: Applications and selection guidelines. *Surface and Coatings Technology*, 38(3):267–280, 1989.

[30] J. R. Creighton and P. Ho. Introduction to chemical vapor deposition (CVD). *Chemical vapor deposition*, 2:1–22, 2001.

[31] E. M. Trent and P. K. Wright. *Metal cutting*. Butterworth-Heinemann, 2000.

[32] R. Colmet and R. Naslain. Chemical vapour deposition of alumina on cutting tool inserts from $AlCl_3$-H_2-CO_2 mixtures: Influence of the chemical vapour deposition parameters and the nature of the inserts on the morphology and wear resistance of the coatings. *Wear*, 80(2):221–231, 1982.

[33] J. G. Kim, C. S. Park, and J. S. Chun. Effect of partial pressure of the reactant gas on the chemical vapour deposition of Al_2O_3. *Thin Solid Films*, 97(1):97–106, 1982.

[34] C. S. Park, J. G. Kim, and J. S. Chun. Crystallographic orientation and surface morphology of chemical vapor deposited Al_2O_3. *Journal of the Electrochemical Society*, 130(7):1607–1611, 1983.

[35] C. S. Park, J. G. Kim, and J. S. Chun. The effects of reaction parameters on the deposition characteristics in Al_2O_3 CVD. *Journal of Vacuum Science & Technology A: Vacuum, Surfaces, and Films*, 1(4):1820–1824, 1983.

[36] M. Kornmann, H. Schachner, R. Funk, and B. Lux. Nucleation of alumina layers on TiC and cemented carbides by chemical vapor deposition. *Journal of Crystal Growth*, 28:259–262, 1975.

[37] S. Vuorinen and J. Skogsmo. Characterization of α-Al_2O_3, κ-Al_2O_3, and α-κ multioxide coatings on cemented carbides. *Thin Solid Films*, 193:536–546, 1990.

[38] M. Halvarsson, H. Nordén, and S. Vuorinen. The microstructure of bonding layers for CVD alumina coatings. *Surface and coatings technology*, 68:266–273, 1994.

[39] C. Chatfield, J. N. Lindström, and M. E. Sjöstrand. Microstructure of CVD-Al_2O_3. *Le Journal de Physique Colloques*, 50(C5):C5–377, 1989.

[40] M. Halvarsson and S. Vuorinen. Microstructural investigations of CVD TiN/κ-Al_2O_3 multilayer coatings on cemented carbides. *International Journal of Refractory Metals and Hard Materials*, 15(1-3):169–178, 1997.

[41] W. H. Gitzen. *Alumina as a ceramic material*. American Ceramic Society, United States, 1970.

[42] L. K. Hudson, C. Misra, A. J. Perrotta, K. Wefers, and F. S. Williams. Aluminum oxide. *Ullmann's Encyclopedia of industrial chemistry*, 2000.

[43] K. Wefers and C. Misra. *Oxides and hydroxides of aluminum*, volume 19. Alcoa Laboratories Pittsburgh, PA, 1987.

[44] I. Levin and D. Brandon. Metastable alumina polymorphs: crystal structures and transition sequences. *Journal of the American ceramic society*, 81(8):1995–2012, 1998.

[45] M. L. Kronberg. Plastic deformation of single crystals of sapphire: basal slip and twinning. *Acta Metallurgica*, 5(9):507–524, 1957.

[46] Y. Kim and T. Hsu. A reflection electron microscopic (REM) study of α-Al_2O_3 (0001) surfaces. *Surface science*, 258(1-3):131–146, 1991.

[47] S. Matthies, G. W. Vinel, and K. Helming. *Standard distributions in texture analysis: maps for the case of cubic-orthorhomic symmetry*, volume 1. Akademie-Verlag, 1987.

[48] H. J. Bunge. Three-dimensional texture analysis. *International Materials Reviews*, 32(1):265–291, 1987.

[49] F. Klocke and A. Kuchle. Cutting tool materials and tools. In *Manufacturing Processes 1*, pages 95–196. Springer, 2011.

[50] P. A. Dearnley. *Surface Engineering for Cutting Tools*, page 324–386. Cambridge University Press, 2017.

[51] K. A. Connors. *Chemical kinetics: the study of reaction rates in solution*. Wiley-VCH Verlag GmbH, 1990.

[52] K. Holmberg and A. Matthews. *Coatings tribology: properties, mechanisms, techniques and applications in surface engineering*. Elsevier, 2009.

[53] G. T. Smith. *Cutting tool technology: industrial handbook*. Springer Science & Business Media, 2008.

[54] M. C. Shaw and J. O. Cookson. *Metal cutting principles*, volume 2. Oxford university press New York, 2005.

[55] ASM Handbook. Friction, lubrication, and wear technology. *ASM International, Materials Park, Ohio*, 18:127–160, 1992.

[56] K. Stjernberg and A. Thelin. Wear mechanisms of coated carbide tools in machining of steel. *High Productivity Machining: Materials and Processes*, pages 95–104, 1985.

[57] D. Hull and D. J. Bacon. *Introduction to dislocations*. Butterworth-Heinemann, 2001.

[58] R. C. Bradt and R. E. Tressler. *Deformation of ceramic materials*. Springer Science Business Media, 2012.

[59] M. F. Ashby. A first report on deformation-mechanism maps. *Acta Metallurgica*, 20(7):887–897, 7 1972.

[60] T. G. Langdon and F. A. Mohamed. A simple method of constructing an Ashby-type deformation mechanism map. *Journal of Materials Science*, 13(6):1282–1290, 6 1978.

[61] G. I. Taylor. The mechanism of plastic deformation of crystals. Part I.—Theoretical. *Proceedings of the Royal Society of London. Series A, Containing Papers of a Mathematical and Physical Character*, 145(855):362–387, 1934.

[62] P. M. Anderson, J. P. Hirth, and J. Lothe. *Theory of dislocations*. Cambridge University Press, 2017.

[63] J. D. Snow and A. H. Heuer. Slip systems in Al_2O_3. *Journal of the American Ceramic Society*, 56(3):153–157, 1973.

[64] D. J. Gooch and G. W. Groves. Non-basal slip in sapphire. *The Philosophical Magazine: A Journal of Theoretical Experimental and Applied Physics*, 28(3):623–637, 1973.

[65] P. D. Bayer and R. E. Cooper. A new slip system in sapphire. *Journal of Materials Science*, 2(3):301–302, 1967.

[66] D. J. Gooch and G. W. Groves. The creep of sapphire filament with orientations close to the c-axis. *Journal of Materials Science*, 8(9):1238–1246, 1973.

[67] R. E. Tressler and D. J. Barber. Yielding and Flow of c-axis Sapphire Filaments. *Journal of the American Ceramic Society*, 57(1):13–19, 1974.

[68] J. B. Bilde-Sørensen, B. F. Lawlor, T. Geipel, P. Pirouz, A. H. Heuer, K. P. D. Lagerlöf, et al. On basal slip and basal twinning in sapphire (α-Al_2O_3)—I. Basal slip revisited. *Acta materialia*, 44(5):2145–2152, 1996.

[69] George Levi, Wayne D Kaplan, and Menachem Bamberger. Structure refinement of titanium carbonitride (TiCN). *Materials Letters*, 35(5-6):344–350, 1998.

[70] Atsutomo Nakamura, Masaya Ukita, Naofumi Shimoda, Yuho Furushima, Kazuaki Toyoura, and Katsuyuki Matsunaga. First-principles calculations on slip system activation in the rock salt structure: Electronic origin of ductility in silver chloride. *Philosophical Magazine*, 97(16):1281–1310, 2017.

[71] J Linckens, G Zulauf, and J Hammer. Experimental deformation of coarse-grained rock salt to high strain. *Journal of Geophysical Research: Solid Earth*, 121(8):6150–6171, 2016.

[72] Jonathan Amodeo, Sébastien Merkel, Christophe Tromas, Philippe Carrez, Sandra Korte-Kerzel, Patrick Cordier, and Jérôme Chevalier. Dislocations and plastic deformation in MgO crystals: a review. *Crystals*, 8(6):240, 2018.

[73] JJ Gilman. Plastic anisotropy of LiF and other rocksalt-type crystals. *Acta Metallurgica*, 7(9):608–613, 1959.

[74] A Taylor and PL Pratt. The transient conductivity increase in deformed alkali halides. *Philosophical Magazine*, 3(33):1051–1052, 1958.

[75] N Li, SK Yadav, X-Y Liu, J Wang, RG Hoagland, N Mara, and A Misra. Quantification of dislocation nucleation stress in TiN through high-resolution in situ indentation experiments and first principles calculations. *Scientific reports*, 5(1):1–8, 2015.

[76] RM Harris and PD Bristowe. Computer modelling of slip in TiC. *Philosophical Magazine A*, 79(3):705–721, 1999.

[77] A. Guinier and D. L. Dexter. *X-ray Studies of Materials*. Number 20. John Wiley & Sons Inc, 1963.

[78] C. Suryanarayana and M. G. Norton. *X-ray diffraction: a practical approach*. Springer Science & Business Media, 2013.

[79] J. I. Goldstein, D. E. Newbury, J. R. Michael, N. W. M. Ritchie, J. H. J. Scott, and D. C. Joy. *Scanning electron microscopy and X-ray microanalysis*. Springer, 2017.

[80] W. Zhou and Z. L. Wang. *Scanning microscopy for nanotechnology: techniques and applications*. Springer science & business media, 2007.

[81] J. K. Farrer, J. R. Michael, and C. B. Carter. EBSD of ceramic materials. In *Electron Backscatter Diffraction in Materials Science*, pages 299–318. Springer, 2000.

[82] O. Engler and G. Gottstein. A new approach in texture research: local orientation determination with EBSP. *steel research*, 63(9):413–418, 1992.

[83] R. R. Keller and R. H. Geiss. Transmission EBSD from 10 nm domains in a scanning electron microscope. *Journal of Microscopy*, 245(3):245–251, 2012.

[84] P. W. Trimby. Orientation mapping of nanostructured materials using transmission Kikuchi diffraction in the scanning electron microscope. *Ultramicroscopy*, 120:16–24, 2012.

[85] G. C. Sneddon, P. W. Trimby, and J. M. Cairney. Transmission Kikuchi diffraction in a scanning electron microscope: A review. *Materials Science and Engineering: R: Reports*, 110:1–12, 2016.

[86] D. B. Williams and C. B. Carter. *Transmission Electron Microscopy: A Textbook for Materials Science. Diffraction. II*, volume 1. Springer Science & Business Media, 1996.

[87] R. F. Egerton et al. *Physical principles of electron microscopy*, volume 56. Springer, 2005.

[88] L. A. Giannuzzi et al. *Introduction to focused ion beams: instrumentation, theory, techniques and practice*. Springer Science & Business Media, 2004.

[89] Baptiste Gault, Michael P Moody, Julie M Cairney, and Simon P Ringer. *Atom probe microscopy*, volume 160. Springer Science & Business Media, 2012.

[90] Michael K Miller. *Atom probe tomography: analysis at the atomic level*. Springer Science & Business Media, 2012.

[91] Michael K Miller and Richard G Forbes. The local electrode atom probe. In *Atom-Probe Tomography*, pages 229–258. Springer, 2014.

[92] H. Schaeben, R. Hielscher, and F. Bachmann. Texture Analysis with MTEX – Free and Open Source Software Toolbox. In *Texture and Anisotropy of Polycrystals III*, volume 160 of *Solid State Phenomena*, pages 63–68. Trans Tech Publications, 2010.